ROTATING LINE CAMERAS: IMAGE QUALITY CONTROL AND CAMERA DESIGN

By

Shou Kang Wei

Fay Huang

and

Reinhard Klette

IMA Preprint Series # 2110

(March 2006)

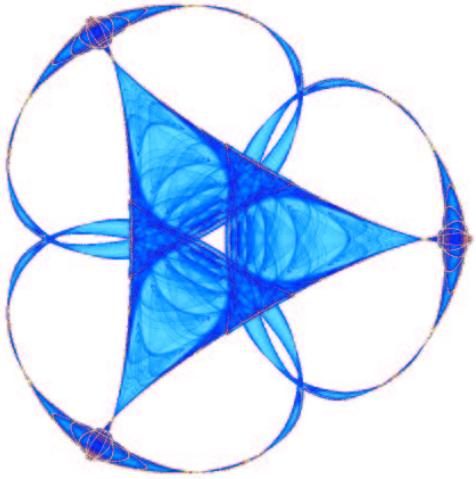

INSTITUTE FOR MATHEMATICS AND ITS APPLICATIONS

UNIVERSITY OF MINNESOTA

400 Lind Hall
207 Church Street S.E.
Minneapolis, Minnesota 55455–0436

Phone: 612/624-6066 Fax: 612/626-7370
URL: http://www.ima.umn.edu

Rotating Line Cameras: Image Quality Control and Camera Design

Shou Kang Wei, Fay Huang, and Reinhard Klette

Taipei and Auckland

Abstract. Rotating line cameras allow to modify camera parameters for adjusting numbers of potential spatial samples within a defined region of interest. The report studies relations between camera parameters and scene parameters, and derives a general approach for designing stereo panoramic cameras. The report also provides a list of problems for further research

Acknowledgment. The authors acknowledge comments, collaboration or support by various students and colleagues at CITR Auckland and DLR Berlin-Adlershof.

INTRODUCTION

This report and its two predecessors, (Huang et al., 2006) and (Huang et al., 2006a), discuss original approaches to two common problems in computer vision, photogrammetry or 3D visualization, namely camera calibration and stereo geometry (epipolar geometry, stereoacuity, maximizing depth layers, and so forth), with respect to a general model of a cylindric panoramic camera, which is basically defined by one or several rotating line sensors.

1.1. Camera Model

The proposed camera model [see (Huang et al., 2006); we do not repeat definitions in this report] unifies various existing models of panoramic cameras into a single and more general representation. As a consequence, studies based on this general model uncover basic properties of panoramic imaging.

The camera model covers single-center as well as multiple-center projections. With this feature, it allows flexibilities for acquiring various types of panoramic images, such as stereo panoramas, leveled panoramas, and traditional, widely used single-center panoramas. Our approach towards multiple panoramas contributes to the discussion of human stereo vision-related processes in camera design, camera parameter selection, camera calibration, or epipolar geometry.

Multiple panoramas can be classified into just a few classes based on their geometric configurations. These classes include single-center, polycentric, parallel-axis, leveled, co-axis, concentric, and symmetric panoramas. Each class has its own theoretical or practical merits and characteristics, which have been discussed in our first two IMA reports. Among all the classes, the polycentric panorama model represents the most general category. Geometric studies based on this model are useful not only for exploring geometric behaviors of multiple panoramas in a general sense, but also for studies of more specific types of multiple panoramas, such as parallel-axis, leveled, co-axis, concentric panoramas etc.

Leveled panoramas are one of the interesting cases studied in our reports, and it is expected that this multi-panorama model attracts more studies in the future. It offers many practical advantages such as a "natural" orientation, a maximization of common fields of view, reliability, and reduction in dimensionality. By distributing locations of captured panoramas within a certain region following this leveled geometric configuration, one collects representative visual information of scenes, and therefore possesses higher probabilities for accurate scene reconstructions compared with the unleveled case.

In this report we assume that the base circle of a panoramic camera is a perfect circle. However, in some situations, this assumption might fail, especially when using a progressive scanning approach, or even allowing (line) camera motion during image capturing. An elliptical or a star-shaped *base curve* may replace the base circle in the more general studies. Moreover, for generalizing the image surface (i.e., the image cylinder in our studies), consider the case when the optical axis of the camera is not always perfectly incident with the base plane (e.g., a conic image surface may be obtained instead of a cylinder). Such a conic distortion of the image surface might be due to some minor camera defects, or due to very high resolutions of line cameras [for example, 10,200 pixels per line in EyeScan, see (Scheibe et al., 2001)] which may justify this problem for even "very minor" (at the first glance) camera defects. In general, studies on extensions of our camera model with respect to base curve and image surface might be of interest for future camera design.

Although many different panoramic camera models have been proposed in the literature, there is still a lack of studies on formal principles which are essential for the design and the assessment of camera architectures.

1.2. Analysis of Epipolar Geometry

The study of epipolar geometry [see (Huang et al., 2006a)] is essential for applications such as 3D scene reconstruction from panoramic images, visualization, or simulation of walk-throughs (i.e., where virtual paths are created between multiple panoramas). The provided general epipolar curve equation serves as a fundamental tool for a diversity of computer vision tasks, such as pose estimation or stereo analysis. Interestingly, we also realized that it is possible to use the epipolar curve equation together with (correct) information on image correspondences for camera calibration.

The general epipolar curve equation for cylindric panoramas, as published in (Huang et al., 2001b), is applicable to all types of cylindric panoramas. We demonstrated how simplified epipolar curve equations are derived for specific pairs of panoramas, such as leveled, co-axis, or symmetric

panoramas.

In the planar (or pinhole) image case there is a one-to-one correspondence between epipolar lines in both images of an image pair, and epipolar lines only intersect at an epipole. There is in general no one-to-one correspondence between epipolar curves, for a pair of polycentric panoramic images, except for the special cases of single-center or symmetric panoramas. Epipolar curves in a polycentric pair (normally) cross each other, and these intersections are not necessarily at epipoles.

The general epipolar curve equation is rather complicated due to the geometric complexity of the cylindric panoramic camera model. Our panoramic camera model uses a Cartesian coordinate system that allows that camera orientation or position are described in a simple and linear manner, with respect to the Cartesian world coordinate system. However, the choice of this coordinate system increases the complexity of the projection formula by involving rather complicated trigonometric expressions. Thus, exploring some other possible alternatives of algebraic representations in order to simplify representations may be another subject for future studies. Nevertheless, we believe that our polycentric model is more appropriate for describing a pair of 'uncalibrated' cylindric panoramas than an oversimplified model such as that of single-center panoramas. As a reason, in practice, it is difficult to ensure that the camera's nodal point is perfectly on the rotation axis during panorama acquisition.

There are several parameters involved in the general epipolar curve equation. It is of interest to investigate how each of them affects the behavior of the epipolar curves. The investigation may proceed into the following directions: One of them is the error sensitivity analysis, which can be carried

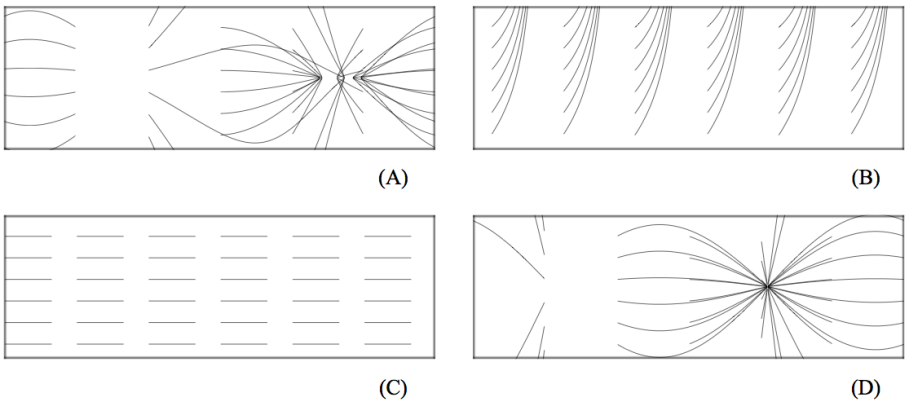

Figure 1.1. Epipolar curves of four special cases: (A) leveled; (B) concentric; (C) symmetric; and (D) single-center panoramas.

out by introducing an error to each parameter and measuring the differences between actual and ideal image projections. The results are useful for improving the robustness of estimating epipolar geometry as well as for stereo analysis. Another possible future direction is the characterization of epipolar curves according to their features, such as intersection, curvature, and so forth. In this case, the features might be expressed in different representations so that the computational complexity of epipolar curves could be reduced. Furthermore, a possible future direction is the classification of different patterns of epipolar curves. Figure 1.1 illustrates the distinctiveness of epipolar curve patterns in four discussed geometric configurations: leveled; concentric; symmetric; and single-center panoramas. The classification will be important to the applications of epipolar geometry recovery or pose estimation in an uncalibrated situation, because, given a set of known corresponding image points we may infer which class the panoramic pair belongs to, and thus obtain an initial guess of for values of parameters.

1.3. Camera Calibration

We subdivided the calibration process for a panoramic camera into two steps, see (Huang et al., 2006). The first step calibrates the effective focal length f and the principal row v_c. The second step calibrates two essential panorama-characteristic parameters: off-axis distance R, and principal angle ω. The shown separability of the calibration process proves an intrinsic feature of panoramic camera geometry, to be a mixture of linear and non-linear components.

A main problem in camera calibration is the high dimensionality involved. We presented three different approaches for the second step of panoramic camera calibration. In the first approach, the point-based approach, there are a total of 14 parameters to be estimated, consisting of the target parameters R, ω, and the other twelve unknowns in the transformation matrix, due to the fact that extrinsic camera parameters are unavoidable. The second approach reduces the dimensions down to four by utilizing information from image correspondences between panoramic images and through avoiding the inclusion of extrinsic camera parameters. In the third approach (i.e., the parallel-line-based approach), linear geometric features are used. As a result, only three parameters need to be estimated in this case. Not surprisingly, the third approach gives the best results among all, also verified in our practical experiments.

Another major problem for camera calibration is the complexity of the error function, where high complexity incurs unstable parameter estimation. Our first approach, the point-based approach, involves non-linear

features, such as fractions, square roots, and so forth, and, therefore, results in unstable estimation. The other two approaches, the image correspondence and the parallel-line-based approaches, allow the error functions to be in linear form, and improve the stability of estimation results in comparison to the point-based approach. For the second approach, however, our experimental results show that the estimated values are rather sensitive to errors. One of the possible factors could be that the values of the associated coefficients in the objective function are rather close.

The second approach (i.e., calibration by image correspondence) is of interest since neither measuring in scenes nor any calibration object are required. We thus avoid the inclusion of extrinsic camera parameters into the calibration process. We identified limitations in calibrating parameters R and ω. Our results show that this (second) approach can only calibrate the principal angle ω, and it is unable to recover the actual value of off-axis distance R. Our studies also show that a concentric panoramic configuration (i.e., with different off-axis distances but the same principal angle ω) gives the best performance.

The third approach (which is parallel-line based) allows the most accurate calibration results as well as the best numerical stability among these three approaches. We found that for different geometric properties of parallel lines (distance between lines, angle formed by three lines), there is a single linear equation that links those 3D geometric scene features of parallel lines to the camera model. Therefore, by providing adequate scene measurements, we are then able to calibrate R and ω with good accuracy. The errors in estimated parameters increase linearly with respect to input errors. More specifically, estimated parameters obtained by using an orthogonality constraint are more sensitive to errors than those in the case of using the distance constraint. Overall, the reduction of dimensionality, the simplification of computational complexity, and being less sensitive to errors are attributes of the linear geometric feature approach. It will be of interest to continue these explorations by using further geometric features (e.g., triangles or squares), properties (e.g., point ratios), or 'hybrid features' such that the followings can be achieved: (1) relax the assumption that the rotation axis must be parallel to the calibration lines; (2) improve the robustness to error; and (3) map the current two calibration steps into a single procedure.

Our solutions for both presented cases of the third approach (for calibrating R and ω) are in a closed form. A special characteristic in this relation is that there is a nonlinear constraint among the variables (i.e., further optimization might be possible). Theoretically, three pairs of parallel lines are the minimum requirement for the calibration of R and ω. The relative locations and the lengths of these lines are critical for the accuracy

and numerical stability of the estimation of these two parameters. Thus, the design of a calibration object for panoramic cameras will be an important task in the future (e.g., supporting our third approach).

1.4. This Report

In this report we provide a simple model for a 3D scene, basically defined by four parameters, where three are easy to estimate (or measure) distances, and the fourth is the number of depth levels desired for a particular stereo application.

All notations regarding the camera model are exactly as in (Huang et al., 2006), and will not be redefined in this report.

IMAGE QUALITY CONTROL

Image quality has been addressed in camera developments since the first photo ever was taken by Joseph Nicéphore Niépce (1975–1833) in 1826, when an exposure time of eight hours produced (under today's point of view) a highly unsatisfactory image of parts of farm buildings. Image quality influences substantially the range of possible applications (e.g., in computer vision or photogrammetry); it is of continuous interest in camera design, production, and application. *Image quality* can be specified with respect to capabilities (e.g., speed), geometric or photometric accuracy, or circumstances of acquisition (e.g., against a light source, or on a vibrating bridge), and we refrain from the attempt of a formal definition of image quality.

Consequently, *image quality control* also remains vaguely defined in general terms as a method which identifies proper settings of camera parameters such that image quality meets defined requirements or criteria. Those requirements or criteria (e.g., optimized for a particular 3D scene complexity, or a maximum of spatial stereo samples within a particular range of depth) are specified by the acquisition context. The camera is assumed to be a precisely defined parameterized model, and we do not apply any further constraints for camera parameters (i.e., cameras allow various parameter settings as defined in their model without any impact on image quality). Pinhole or multiple-projection-center panoramic cameras are examples of parameterized camera models.

2.1. Two Requirements

The design of an image quality control method requires the understanding of geometric or photometric relations between given requirements or citeria (defined by the context of image acquisition) and possible parameter settings. Requirements or criteria vary with the architecture of the used camera. This chapter addresses image quality control for two geometric requirements when capturing a scene with a symmetric panoramic camera

(for stereo viewing or stereo reconstruction).

First, the given *scene composition* (here basically defined only by distances between camera and objects in the scene, not by, for example, artistic aspects) should be used for maximizing the number of spatial samples within the "range of interest".

Second, *stereoacuity* should be maximized for an assumed stereo-viewing situation (not, for example, modeling the stereoacuity of individual eyes, but the geometry of the viewing situation) for the captured symmetric panorama.

The first requirement is valid for computational stereo, and its solution contributes also to the satisfaction of the second requirement, which is valid for stereo-viewing applications (e.g., for a 3D cinema).

The stereoacuity problem is to analyze settings of camera parameters in relation to resultant numbers of depth layers. *Proper stereoacuity* for scenes of interest is defined by optimized representations of geometric scene complexities. Insufficient stereoacuity produces a *cardboard effect*, see (Yamanoue et al., 2000), where the 3D scene is perceived as a set of 'parallel cardboards', sorted in depth, one sitting in front of the other. Another case of improper stereoacuity is when greater than the upper disparity limit for human vision; this causes double images, called *dipopia*, which results in uncomfortable stereo viewing as well as eyestrain (Viire, 1997; Siegel et al., 1999; Mayer et al., 2000).

Both quality issues are often mentioned, see (Ishiguro et al., 1992; Shum and He, 1999; Shum et al., 1999; Shum and Szeliski, 1999; Wei et al., 1999a; Peleg and Ben-Ezra, 1999; Peleg et al., 2000; Huang and Pajdla, 2000). However, image quality control is not discussed in these studies. In particular, some approaches as reported in (Shum and He, 1999; Shum et al., 1999; Shum and Szeliski, 1999; Peleg and Ben-Ezra, 1999; Peleg et al., 2000) restrict camera parameters to constant values [e.g., constant principal angle $\omega = 90°$ or $270°$ in (Shum et al., 1999)] or to a specific interval (e.g., $0° \leq \omega \leq 90°$). Under such a-priori restrictions, image quality control becomes difficult or even impossible with respect to both specified requirements.

Panorama acquisition is (still) a time-consuming, storage-consuming[1] and costly[2] process. Without using a proper image quality control method, quality of resultant images cannot be ensured, and hence further acquisi-

[1] One panoramic image as in (Huang et al., 2001) is of 7 GB in raw format; see Figure 2.1 for a low-resolution example. These images were acquired with a line having about 10,000 pixel sensors. Recent line sensor developments go towards double length (i.e., increasing the file size roughly by factor 4 again). A symmetric panorama combines two of such images.

[2] Labor, equipment, transport, insurance etc.; see Figure 2.2.

Figure 2.1. (Huang et al., 2001) reports about the acquisition of images with a rotating line camera in New Zealand, also showing several examples. The figure shows a resolution-reduced part of one of those (single-line) 7 GB panoramas (view from the roof of the Auckland museum).

tions might be required, incurring more costs. On the other hand, we do not want to introduce unnecessarily overheads (e.g., time, costs, or weights) to the original image acquisition process or device. An image quality control method has to be time-efficient and simple to handle.

This chapter describes an image quality control method for the two selected criteria. We provide a formula how to optimize camera parameters (such as off-axis distance R, principal angle ω, or angular unit γ) for the acquisition of symmetric panoramas. Section 2.2 is about basic geometric relationships between parameterized panoramic camera, range of interest in the 3D scene, and further application requirements. This section leads to a more precise formulation of the image quality control problem. Section 2.3 presents a solution for this problem by computing optimized values for camera parameters. A few examples demonstrate the practical use of the derived formulas. Section 2.4 discusses how measurement errors (which cannot be totally excluded) may (still) impact image quality, assuming that our image quality control method has been used for parameter adjustment.

Figure 2.2. Personal and equipment of a panoramic imaging project, reported in (Huang et al., 2001). Due to the size of the images, the acquisition of a few images was quickly filling the hard disk of a PC.

2.2. Geometry between Camera and 3D Scene

2.2.1. RANGE OF INTEREST IN THE SCENE

A *range of interest* (*RoI* for brevity) is defined as a volume between two concentric cylinders; see Figure 2.3. The inner cylinder (radius D_1) is defined by closest objects of interest, and the outer cylinder (radius D_2) by furthest objects of interest. (We assume that $D_1 \neq D_2$.) The *height* V_1 ("V" for "vertical") of a RoI is estimated at the inner cylinder.

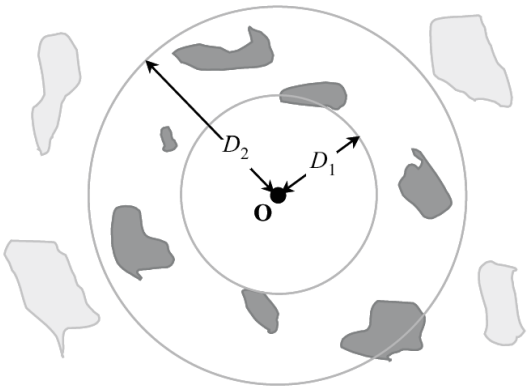

Figure 2.3. Top view of a RoI. Darker objects indicate locations which are of (major) interest while light-gray areas are not, or of minor interest. The figure indicates that both radii are in practice just estimated based on 2.5D visibility (with respect to **O**) of objects of interest.

This model of a RoI corresponds to the spatial sampling structure of symmetric panoramas. The goal is to have accurate distance values (in computational stereo) or optimized stereo visualization within a given RoI.

Let φ be the angle which specifies the vertical (angular) field of view, defined by the given or chosen lens of the camera. We have the following:

$$V_1 = 2H_1 \tan(\frac{\varphi}{2}) \tag{1}$$

where H_1 is the distance between a focal point **C** (of a line image) and the point where that projection ray which is incident with the base plane intersects the inner cylinder (of radius D_1); see Figure 2.4(A). H_1 depends on ω and R, but not on a particular line image (of index i, $1 \leq i \leq W$).

A measurement of height V_1 is more difficult in practice than a measurement of H_1. Thus we use H_1 and φ to describe the height of a RoI. The measurement (or estimation) of distances to furthest or nearest objects of interest defines the input for our quality control method, and various tools

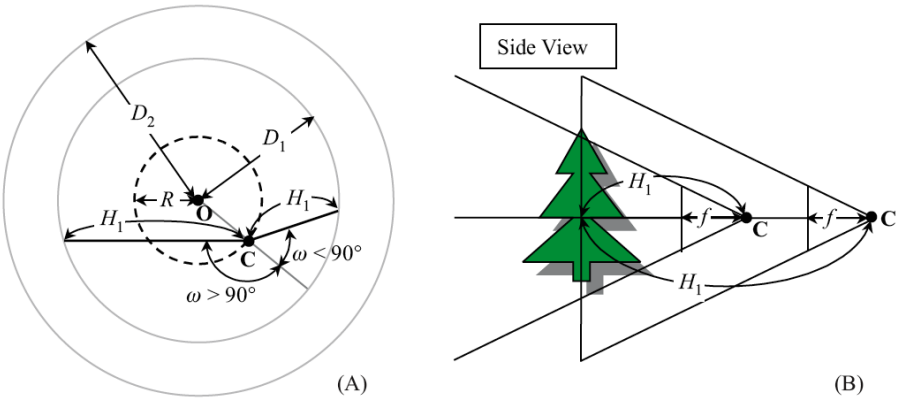

Figure 2.4. (A) Top view of a RoI: off-axis distance R remains constant, but ω is shown for an inward and an outward case; both cases define different values of H_1. (B) Side view: both values of H_1 define different values of height V_1 at the inner cylinder.

can be used (e.g., a laser range finder or a GPS for larger distances). The value of H_1 should be larger than the shortest focusable distance, and it will be smaller than $2D_1$.

If D_1 is small, typically a wide-angle lens would be chosen. Note that H_1 (based on angle ω) allows to increase the distance to the inner cylinder of the RoI, that means there is a reduced need for a wide-angle lense (which causes more lens distortion).

The positioning of the camera within the inner cylinder is typically very much constraint by the given scenery (architecture, landscape, etc.). Thus we do not discuss further optimization at this point, and simply take the camera position as a predefined input.

2.2.2. DEPTH, DISPARITY, AND ANGULAR DISPARITY

All spatial samples of a symmetric panorama (see Theorem 6.1) are in general partially inside of a given RoI, and partially outside. The aim is to maximize the number of depth layers between D_1 and D_2.

We use two different representations of depth layers; one is specified by *angular disparity* θ, which is defined by the angle (centered at **O**) between two corresponding points (on the image cylinder) in the left and right panorama of a symmetric panorama; see Figure 2.5. The figure illustrates a symmetric panorama and two points in 3D space, one on the inner and one on the outer cylinder of the RoI. Both points define angular disparities θ_1 and θ_2, and the *width of the angular disparity interval* is defined by $\theta_w = \theta_2 - \theta_1$. Angular disparities allow to represent depth layers.

A second representation is specified by *disparity* d, which is defined by

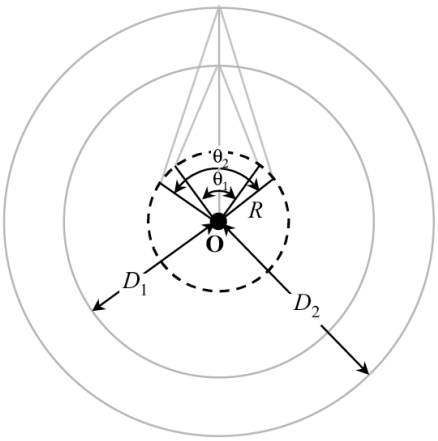

Figure 2.5. Two angular disparities θ_1 and θ_2 , defined by (arbitrary) 3D points on the inner and outer cylinder of the shown RoI.

the *horizontal parallax* (i.e., the difference in positions between two corresponding points in the left and right panorama, measured in the number of image colums between both on the image cylinder). Let d_1 or d_2 be disparities for 3D points on the inner or outer cylinder of a RoI, respectively. The *width of the disparity interval* is defined by $d_w = d_2 - d_1$. (Note that disparities are one-dimensional for symmetric panoramas.)

Obviously, disparity and angular disparity are related as follows:

$$\theta = \frac{2\pi d}{W} \tag{2}$$

where W is the width of the symmetric panorama in pixels. Valid ranges of θ and d are $0^\circ < \theta < 180^\circ$ and $0 < d < \frac{W}{2}$.

The depth D of a 3D point (i.e., the Euclidean distance between point and **O**) is defined by either angular disparity or disparity, assuming R and ω are known. We have the following:

$$D = \frac{R \sin\omega}{\sin\left(\omega - \frac{d\pi}{W}\right)} = \frac{R \sin\omega}{\sin\left(\omega - \frac{\theta}{2}\right)}$$

This formula is of analogous simplicity as the depth formula of standard stereo geometry in the pinhole case.

We define now *stereoacuity* in mathematical terms as the number of those depth layers having a non-empty intersection (in terms of spatial samples) with a given RoI. Maximization of stereoacuity is appropriate for computational stereo.

Stereo viewing also requires that disparities for a RoI stay below the maximum disparity limit for human stereo fusion, which is suggested in

(Valyrus, 2004) as being approximately equal to

$$0.03 \times \text{ viewing distance}$$

This value corresponds to discussions of "fusibility" of corresponding points in other references; see (Howard and Rogers, 1995) for particular viewing conditions, or (Roberts and Slattery, 2000; Ware et al., 1998) for viewing distances in relation to the size of a computer screen. For example, consider stereo-viewing on a 17" screen with a resolution of 1024×768 pixel, and a frontal position in $40cm$ distance, then the upper disparity limit is approximately $d \approx 70$ pixel for fusible and comfortable stereo-viewing (Siegel and Nagata, 2000).

Calculations based on the upper disparity limit, as suggested in (Valyrus, 2004) (see above), also lead to this value of $d \approx 70$ pixel. Interestingly, see (Howard and Rogers, 1995), this upper disparity limit remains about constant for both crossed or uncrossed disparity fields (Figure 2.6 illustrates the definition of crossed or uncrossed disparities.)

Examples in the following, involving the upper disparity limit, use the estimate of (Valyrus, 2004). (We are aware that there is still a lack in

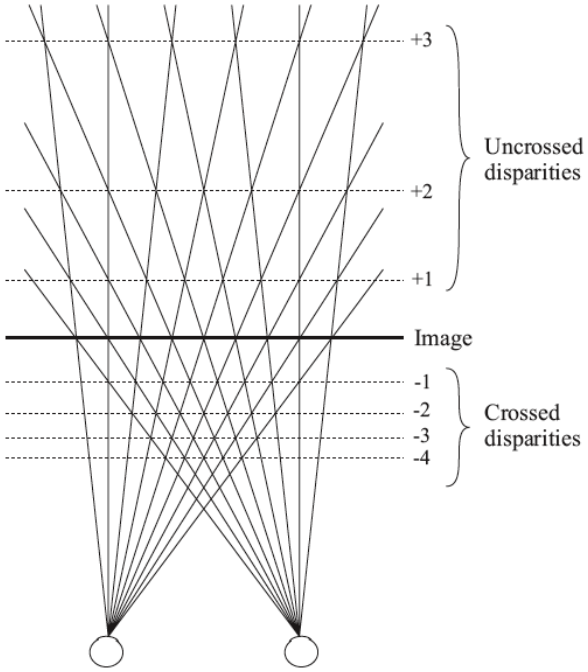

Figure 2.6. The human eye may fuse corresponding points as being in front of the fixation plane (crossed disparities) or behind the fixation plane (uncrossed disparities).

full understanding of human vision with respect to the enormous variety of binocular fusibility and viewing conditions, and there are still limited insights into related characteristics of computer displays.) This implies that it is still difficult to ensure proper stereoacuity, for different viewers and different displays. This also limits our considerations on image quality control for stereo-viewing.

The accuracy of computational stereo is always limited by the stereoacuity available for a symmetric panorama within the RoI, regardless of the performance of the chosen stereo matching algorithm.

2.2.3. IMAGE RESOLUTION

In difference to single-center panoramic acquisition [see, for example, (Chen, 1995; McMillan and Bishop, 1995a; Kang and Weiss, 1997)], where the number W of image columns can be chosen independently from the given 3D scene complexity, the number of image columns of a symmetric panorama should be chosen in dependency of the geometric relationship between the parameterized camera and the given RoI. The geometric relation between camera and RoI was studied for the first time in (Wei et al., 2002a).

Figure 2.7 illustrates our geometric model for computing the number of image columns W of a symmetric panorama. Without loss of generality assume a depth layer exactly at distance D_1; the inner cylinder of the RoI is selected be the *uniform sampling target*, where U is the *ground*

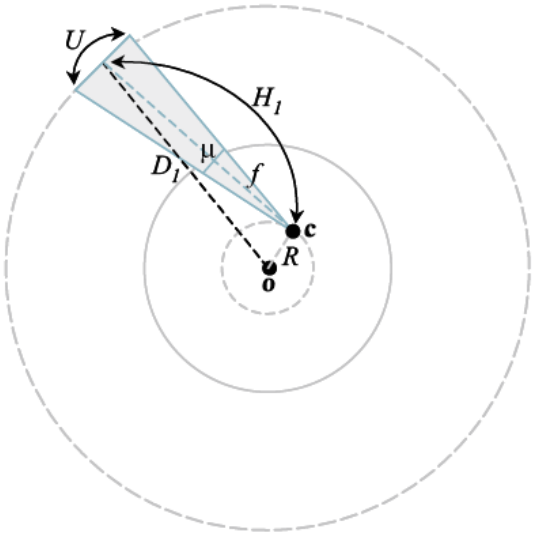

Figure 2.7. Geometric model for computing the number of image columns W of a symmetric panorama.

sampling distance (GSD, defined by the chosen effective focal length f) on this sampling target. A first (and simple) observation is that

$$W = \frac{2\pi D_1}{U} \tag{3}$$

in case of a 360° panorama. Given an effective focal length f, pixel size μ, and the measurement of the corresponding value H_1, Equation (3) can be rewritten as

$$W = \frac{2\pi D_1}{U} = \frac{2\pi f D_1}{H_1 \mu} = \frac{2\pi f}{\mu} \frac{D_1}{H_1} \tag{4}$$

$\frac{2\pi f}{\mu}$ is the horizontal sampling rate for the single-center panorama case, and $\frac{D_1}{H_1}$ characterizes the potential difference to single-center (i.e., $R = 0$ with $D_1 = H_1$) panoramas.

In case of a single-center panorama, the number of projected points (at distance D_1, or wherever projection rays hit a surface) is simply defined by f and μ. Values $R > 0$ and $\omega \neq 0$ ensure that $H_1 > D_1$, what also means that a lens of larger focal length can be used without increasing W.

The image width W limits the total number of possible samples in 3D space, which is equal to

$$W \times H \times \left\lfloor \frac{\omega W}{180^\circ} \right\rfloor$$

For example, in experiments with the WAAC camera [as described in (Reulke and Scheele, 1998); for example, with $H = 5184$ pixel and $\mu = 0.007mm$] we had a lens with $f = 21.7mm$, and thus $W \leq 19,478$ pixel with larger values of W for ω close to zero (which reduces the total number of spatial samples). An indoor RoI could have, for example, $D_1 = 6m$, and thus $H_1 < 12m$ and $W > 9,739$ pixel, for $R < D_1$ and arbitrary ω. The value of W is reduced (for fixed f) when ω goes to 180°, but this may still allow to maximize the total number of spatial samples.

2.3. Parameter Optimization

The optimization problem is for computational stereo defined by the aim of maximizing the number of spatial samples in the given RoI; for stereo-viewing we also have to stay below the upper (angular) disparity limit. Values of the four parameters D_1, D_2, H_1, and θ_w are assumed as input. For computational stereo, the upper angular disparity limit θ_w can be chosen, but cannot be larger than 180°.

2.3.1. OFF-AXIS DISTANCE R AND PRINCIPAL ANGLE ω

Figure 2.8 illustrates symbols and geometric relations as used in this subsection. Let $\mathbf{P}_1$ or $\mathbf{P}_2$ be two 3D points at depth D_1 or D_2, respectively, such that $\mathbf{P}_1$, $\mathbf{P}_2$, and $\mathbf{O}$ are collinear. The circle $\mathcal{H}$, centered at point $\mathbf{P}_1$ of

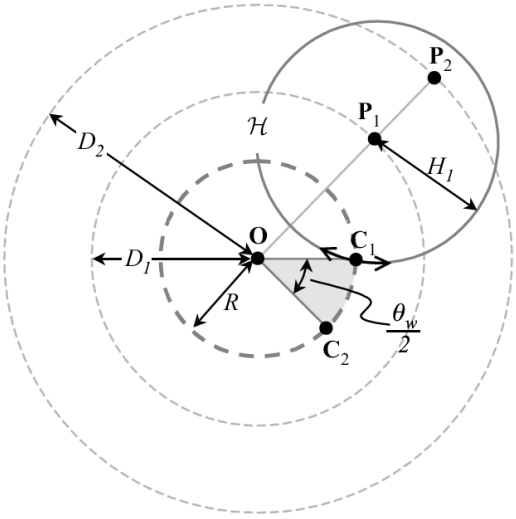

Figure 2.8. Geometric situation when optimizing R and ω.

radius H_1, defines possible locations of optical centers of the camera when acquiring $\mathbf{P}_1$.

Points $\mathbf{P}_1$ or $\mathbf{P}_2$ are projected onto image columns associated to the optical centers at $\mathbf{C}_1$ or $\mathbf{C}_2$, respectively. (The image cylinder is not shown in the figure.) Consequently, the angle defined by line segments $\overline{\mathbf{C}_1\mathbf{O}}$ and $\overline{\mathbf{C}_2\mathbf{O}}$ has to be upper bounded by $\frac{\theta_w}{2}$; see Figure 2.8. We also have that $\angle\mathbf{O}\mathbf{C}_1\mathbf{P}_1 = \angle\mathbf{O}\mathbf{C}_2\mathbf{P}_2$.

THEOREM 2.1. *There exists a unique solution for R and ω which maximizes the number of spatial samples in the RoI and satisfies the upper disparity limit (i.e., angular disparity less or equal θ_w); it is as follows:*

$$R = \sqrt{D_1^2 + H_1^2 + 2D_1H_1\frac{D_1 - D_2\cos\left(\frac{\theta_w}{2}\right)}{\sqrt{A}}}$$

$$\omega = \arccos\left(\frac{D_1D_2\cos\left(\frac{\theta_w}{2}\right) - D_1^2 - H_1\sqrt{A}}{R\sqrt{A}}\right)$$

where $A = D_1^2 + D_2^2 - 2D_1D_2\cos\left(\frac{\theta_w}{2}\right)$.

Proof We show that we can fully utilize the maximum number of depth layers [as defined by the relation in Equation (2)]; obviously this defines the maximum of possible spatial samples.

Consider the triangles $\triangle \mathbf{OP}_1\mathbf{C}_1$ and $\triangle \mathbf{OP}_2\mathbf{C}_2$ in Figure 2.9. By rotating the first one clockwise around $\mathbf{O}$, with rotation angle $\frac{\theta_w}{2}$, point $\mathbf{C}_1$ coincides with $\mathbf{C}_2$. The result is shown in Figure 2.10.

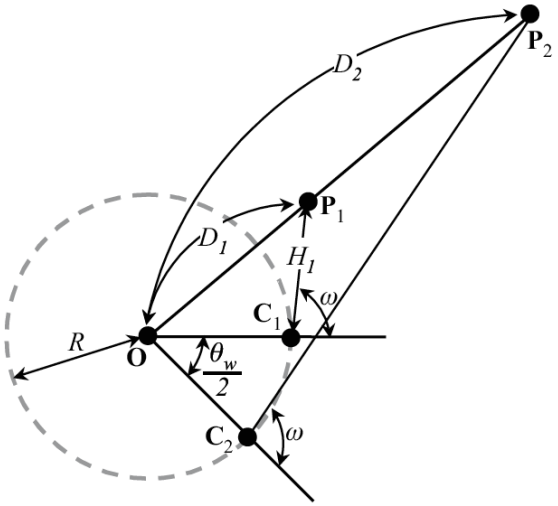

Figure 2.9. Initial geometric situation for the calculation of R and ω.

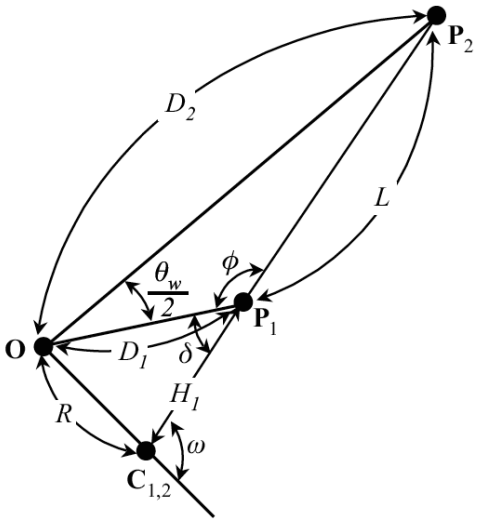

Figure 2.10. Geometric situation after rotation.

Let angle $\angle \mathbf{OP}_1\mathbf{P}_2$ be denoted by ϕ, and angle $\angle \mathbf{OP}_1\mathbf{C}_2$ be denoted by δ. Obviously, $\delta = (180^\circ - \phi)$. Consider $\triangle \mathbf{OP}_1\mathbf{P}_2$ in Figure 2.10; the length L of side $\overline{\mathbf{P}_1\mathbf{P}_2}$ can be calculated by the following formula:

$$L = \sqrt{D_1^2 + D_2^2 - 2D_1 D_2 \cos\left(\frac{\theta_w}{2}\right)} \tag{5}$$

Continue to consider $\triangle \mathbf{OP}_1\mathbf{P}_2$ in Figure 2.10; angle ϕ has the following relationship with the three sides of this triangle:

$$D_2^2 = D_1^2 + L^2 - 2D_1 L \cos\phi$$

This implies that

$$\cos\phi \;=\; \frac{D_1^2 + L^2 - D_2^2}{2D_1 L} \tag{6}$$

Now substitute the formula for L of Equation (5) into Equation (6). We obtain the following:

$$\begin{aligned} \cos\phi \;&=\; \frac{D_1^2 + D_1^2 + D_2^2 - 2D_1 D_2 \cos\left(\frac{\theta_w}{2}\right) - D_2^2}{2D_1\sqrt{D_1^2 + D_2^2 - 2D_1 D_2 \cos\left(\frac{\theta_w}{2}\right)}} \\ &=\; \frac{D_1 - D_2 \cos\left(\frac{\theta_w}{2}\right)}{\sqrt{D_1^2 + D_2^2 - 2D_1 D_2 \cos\left(\frac{\theta_w}{2}\right)}} \end{aligned} \tag{7}$$

The angle δ is defined to be equal to $(180^\circ - \phi)$, thus we have

$$\begin{aligned} \cos\delta \;&=\; \cos(180^\circ - \phi) \\ &=\; -\cos\phi \end{aligned} \tag{8}$$

Next we consider $\triangle \mathbf{OP}_1\mathbf{C}_2$ in Figure 2.10. The value of R can be calculated using the following formula:

$$R = \sqrt{D_1^2 + H_1^2 - 2D_1 H_1 \cos\delta}$$

Summarizing the results of Equations (7) and (8), the value of R can be obtained as follows:

$$R = \sqrt{D_1^2 + H_1^2 + 2D_1 H_1 \frac{D_1 - D_2 \cos\left(\frac{\theta_w}{2}\right)}{\sqrt{D_1^2 + D_2^2 - 2D_1 D_2 \cos\left(\frac{\theta_w}{2}\right)}}} \tag{9}$$

Angle ω satisfies in $\triangle \mathbf{OP}_1\mathbf{C}_2$ the following equation:

$$\begin{aligned} D_1^2 \;&=\; R^2 + H_1^2 - 2RH_1 \cos(180^\circ - \omega) \\ &=\; R^2 + H_1^2 + 2RH_1 \cos\omega \end{aligned}$$

This implies that

$$\omega \;=\; \arccos\left(\frac{D_1^2 - H_1^2 - R^2}{2H_1 R}\right) \tag{10}$$

We substitute the formula for R in Equation (9) into the equation of ω in Equation (10), and obtain the following:

$$\begin{aligned}
\omega \;&=\; \arccos\left(\frac{D_1^2 - H_1^2 - D_1^2 - H_1^2 - 2D_1H_1\frac{D_1 - D_2\cos\left(\frac{\theta_w}{2}\right)}{\sqrt{D_1^2+D_2^2-2D_1D_2\cos\left(\frac{\theta_w}{2}\right)}}}{2H_1\sqrt{D_1^2 + H_1^2 + 2D_1H_1\frac{D_1 - D_2\cos\left(\frac{\theta_w}{2}\right)}{\sqrt{D_1^2+D_2^2-2D_1D_2\cos\left(\frac{\theta_w}{2}\right)}}}}\right) \\
&=\; \arccos\left(\frac{-H_1 + \frac{D_1D_2\cos\left(\frac{\theta_w}{2}\right)-D_1^2}{\sqrt{A}}}{\sqrt{\frac{(D_1^2+H_1^2)\sqrt{A}+2D_1^2H_1-2D_1D_2H_1\cos\left(\frac{\theta_w}{2}\right)}{\sqrt{A}}}}\right) \\
&=\; \arccos\left(\frac{D_1D_2\cos\left(\frac{\theta_w}{2}\right) - D_1^2 - H_1\sqrt{A}}{\sqrt{(D_1^2 + H_1^2)A + 2D_1H_1(D_1 - D_2\cos\left(\frac{\theta_w}{2}\right))\sqrt{A}}}\right)
\end{aligned} \tag{11}$$

where $A = (D_1^2 + D_2^2 - 2D_1D_2\cos\left(\frac{\theta_w}{2}\right))$.

The values of parameters D_1, D_2, H_1, and θ_w have to satisfy the physical constraints as specified in Section 2.2; Equations (9) and (11) then allow to conclude that solutions for R and ω are unique. □

COROLLARY 2.1. *In the computational-stereo case of $\theta_w = 180°$, the unique solution for R and ω simplifies to*

$$\begin{aligned}
R \;&=\; \sqrt{D_1^2 + H_1^2 + 2D_1^2\frac{H_1}{\sqrt{A}}} \\
\omega \;&=\; \arccos\left(\frac{-D_1^2 - H_1\sqrt{A}}{R\sqrt{A}}\right)
\end{aligned}$$

where $A = D_1^2 + D_2^2$.

The possible range of R is $0 < R < D_1$. However, practically the value of R is limited by the provided equipment [e.g., at most $1.0m$ in (Huang et al., 2001)]. For the solution of ω, only the interval of $0° < \omega < 180°$ needs to be considered (for the right camera of the symmetric panorama). If the value of ω is the solution (for the right camera), then $(360° - \omega)$ is

the solution for the left camera. The extreme cases of $R = 0$, or $\omega = 0°$ or $\omega = 180°$ do not support capturing of a stereoscopic panoramic pair (i.e., the number of depth layers and the width of the disparity interval are zero in these cases).

The unique solution is for both parameters. This implies that neither R nor ω can optimize numbers of spatial samples alone. On the other hand, assuming that, for example, R is fixed for a given panoramic camera, but ω is variable, then this allows to define a "viewfinder" for a stereoscopic panoramic camera: different values of ω correspond to different RoIs.

2.3.2. EXAMPLES

We demonstrate results of control values for R and ω for four commonly occurring situations: (1) a close-range indoor scene covering an area of about $36m^2$, (2) a far-range indoor scene of an area of about $400m^2$, (3) an outdoor scene with a RoI with radii of 6 or 50 meters, and (4) an outdoor scene with radii of 20 or 200 meters. For detailing these examples, a floor plan and aerial images are provided in Figures 2.11 and 2.12.

Results for R and ω are shown in Table 2.1. The used camera [WAAC, see (Reulke and Scheele, 1998)] is as specified in Subsection 2.2.3, with an effective focal length of $f = 21.7mm$, pixel size $\mu = 0.007mm$, image height $H = 5,184$ pixel (i.e., values of W follow accordingly for the four examples), an assumed 17" display screen (with 1024×768 pixel) for stereo-viewing at

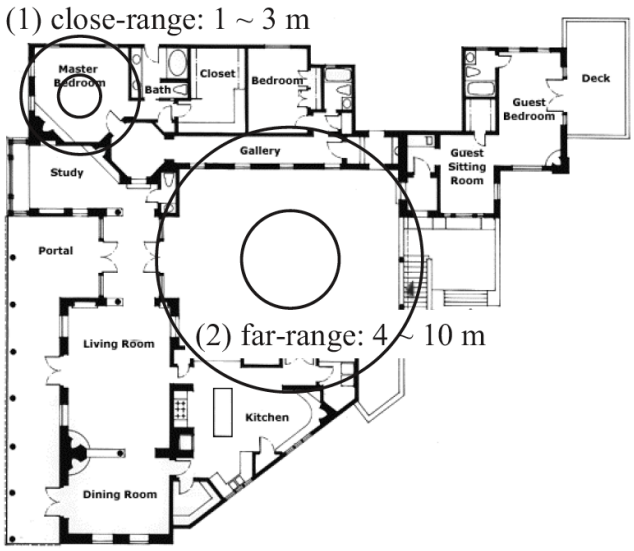

Figure 2.11. Example of a floor plan: case (1) is a close-range indoor scene (top left corner), and case (2) a far-range indoor scene.

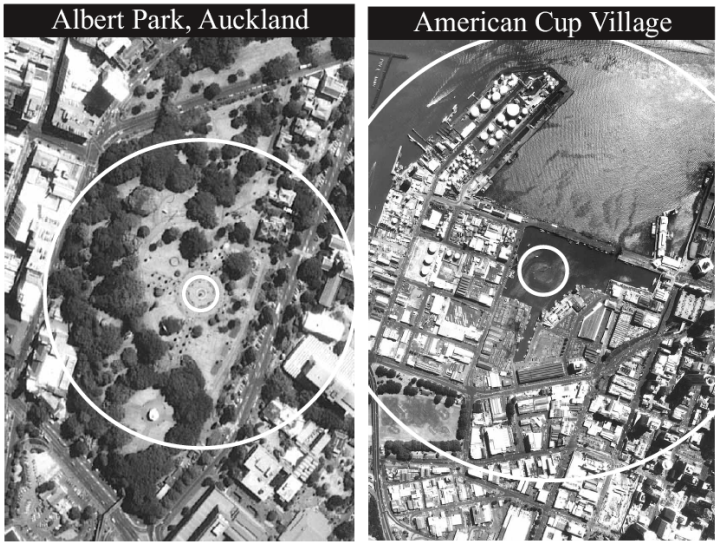

Figure 2.12. Two aerial views (captured by the digital WAAC) of central Auckland: case (3) is a close-range outdoor scene (in Albert Park), and case (4) a far-range outdoor scene (America's Cup Village in 2001).

40cm distance (frontal and centered position of viewer). Input parameters D_1, D_2, and H_1 are measured (estimated) in meters, as is the resulting value of R; θ_w and ω are given in degrees, and W in pixel.

To allow for comfortable stereo-viewing under the specified conditions

	D_1	D_2	H_1	W	θ_w	R	ω
(1)	1	3	1.2	16232	10.48	0.2499	146.88
(2)	4	10	4.2	18550	9.17	0.5809	113.92
(3)	6	50	5.5	21249	8.00	0.6768	44.66
(4a)	20	200	20.0	19478	8.74	1.6942	92.43
(4b)	20	200	20.0	19478	5.00	0.9695	91.39
H_P = 5184 (pixels) u = 0.007 (mm) H_S = 768 (pixels) f = 21.7 (mm)							

Table 2.1. Calculated values for R and ω using Theorem 2.1. We assume stereo-viewing on a screen (resulting into a disparity limit of 70 pixel) and the four examples in Figures 2.11 and 2.12. Case (4b) is defined by the additional constraint that R is limited to be 1.0m at most.

(let $H_S = 768$), Equation (2) becomes

$$\theta_w = \frac{2\pi d_w H}{W H_S}$$

where $d_w = 70$ pixels are used in all four cases for the assumed 17" display. The term $\frac{H}{H_S}$ allows that the acquired vertical perspective is fully rendered on the screen. For interactive zooming within stereoscopic visualization, "stereo-shifts" between left and right panoramic image must be dynamically adapted such that the desired quality of stereo perception is ensured.

Results for R and ω in Table 2.1 show the actual values which correspond to scene composition and optimize stereoacuity.

Values of the principal value ω for the first two examples illustrate typical results for adapting a stereoscopic panoramic camera to indoor conditions. Values $\omega > 90°$ (i.e., the inward case) illustrate the benefit of increasin H_1 compared to D_1.

Values of R computed for examples (1-3) were actually realizable for the setup in (Huang et al., 2001) which allowed $R \leq 1.0m$. Case (4a) leads to a value of R greater than $1.0m$. In this case we demonstrate a tradeoff with stereoacuity: we reduce the value of θ_w from 8.74° to 5.00° (i.e., less spatial samples) and obtain a result with $R < 1.0m$.

2.4. Error Analysis

Measurements (or often just estimations) of the three parameters D_1, D_2, and H_1 (the latter one instead of the more difficult measurement of V_1) are likely to be inaccurate. This section analyzes how errors in these measurements impact the image quality of resultant stereo panoramas. First we define error measures, then we explain parameter dependency for the analysis of error propagation, and finally we provide an error analysis for each of the three input parameter.

2.4.1. DEFINITIONS AND NOTATIONS

We assume three independent errors because of independent measurements of D_1, D_2, and H_1. They are denoted as ε_{D_1}, ε_{D_2}, and ε_{H_1}, respectively, and are real numbers. Measured values of D_1, D_2, and H_1 are $\hat{D}_1 = D_1 + \varepsilon_{D_1}$, $\hat{D}_2 = D_2 + \varepsilon_{D_2}$, and $\hat{H}_1 = H_1 + \varepsilon_{H_1}$. Symbol '^' indicates that a parameter may contain an error, and symbols without '^' stand for true values.

Consequently, calculated parameters based on (potentially inaccurate) measurements are $\hat{R} = R + \varepsilon_R$ and $\hat{\omega} = \omega + \varepsilon_\omega$. These finally effect the disparity interval width $\hat{d}_w = d_w + \varepsilon_{d_w}$ (which characterized stereoacuity in the resultant panorama) or the height $\hat{V}_1 = V_1 + \varepsilon_{V_1}$ (which is a resultant

parameter of the modeled RoI). We analyze how measurement errors are propagating to d_w and V_1.

2.4.2. PARAMETER DEPENDENCIES

In order to study how errors propagate from a measurement to a 'final parameter', we clarify dependencies among used parameters. This subsection lists algebraic dependencies following individual steps during an image acquisition procedure. A functional notation $Y = f_Y(X_1, X_2, \ldots, X_n)$ means that parameter Y potentially depends upon parameters $X_1, X_2, \ldots, X_n$, and (within the scope of this study) upon no others.

The number W of image columns is calculated based on f, μ, D_1, and H_1; see Equation (4). We write this dependency as

$$W = f_W(f, \mu, D_1, H_1)$$

The width θ_w of the angular disparity interval is defined by the width of the image disparity interval d_w and the number of image columns W; see Equation (2). Accordingly we have

$$\theta_w = f_{\theta_w}(d_w, W)$$

Theorem 2.1 defines dependencies between R or ω, and D_1, D_2, H_1, and θ_w. Thus, we also have

$$R = f_R(D_1, D_2, H_1, \theta_w)$$

and

$$\omega = f_\omega(D_1, D_2, H_1, \theta_w)$$

Now consider a case that parameters R and ω are used for the acquisition of a symmetric panorama (e.g., calculated by optimization using the formulas in Theorem 2.1), and the RoI is defined by radii D_1 and D_2. These four parameter values allow to backtrack the (used) values of H_1 and $\theta_w$as follows: for the value of H_1 we have that

$$H_1 = \sqrt{D_1^2 + R^2\cos(2\alpha) + 2R\cos(\alpha)\sqrt{D_1^2 - R^2\sin^2(\alpha)}} \qquad (12)$$

where $\alpha = (180° - \omega)$. In functional notation we express this by the following equation:

$$H_1 = f_{H_1}(D_1, R, \omega)$$

Furthermore, the value of θ_w can be calculated by the following formula:

$$\theta_w = 2\arcsin\left(\frac{R}{D_1 D_2}\sin(\omega)\left[\sqrt{D_2^2 - R^2\sin^2(\omega)} - \sqrt{D_1^2 - R^2\sin^2(\omega)}\right]\right) \qquad (13)$$

Thus, we have

$$\theta_w = f_{\theta_w}(D_1, D_2, R, \omega)$$

Assuming an error free process, the calculated values of H_1 and θ_w should be identical to those values defined by the image acquisition requirements.

For a conversion from (the backtracked) width of the angular disparity interval to width of the image disparity interval, see Equation (2). In more abstract form, we also have

$$d_w = f_{d_w}(\theta_w, W)$$

Similarly, a conversion from (the backtracked) H_1 to the height of the RoI can be obtained through Equation (1); we have

$$V_1 = f_{V_1}(H_1, \varphi)$$

2.4.3. ERROR IN NEAREST SCENE RANGE

$\hat{D}_1$ contains the error ε_{D_1}, and, subsequently, the number of image columns (which depends on D_1) is also erroneous, denoted by $\hat{W}$. Given $\hat{W}$, we obtain $\hat{\theta}_w$ due to the dependency $\hat{\theta}_w = f_{\theta_w}(d_w, \hat{W})$. Both parameters R and ω in Equations (9) and (11) depend on D_1, D_2, H_1 and θ_w. Thus, the erroneous values $\hat{W}$ and $\hat{\theta}_w$ cause erroneous values $\hat{R}$ and $\hat{\omega}$, and the (additive) errors are defined, respectively, as

$$\begin{aligned} \varepsilon_R &= \hat{R} - R \\ &= f_R(\hat{D}_1, D_2, H_1, \hat{\theta}_w) - f_R(D_1, D_2, H_1, \theta_w) \end{aligned}$$

and

$$\begin{aligned} \varepsilon_\omega &= \hat{\omega} - \omega \\ &= f_\omega(\hat{D}_1, D_2, H_1, \hat{\theta}_w) - f_\omega(D_1, D_2, H_1, \theta_w) \end{aligned}$$

The actual width of the angular disparity interval for an acquired symmetric panorama, using determined control values $\hat{R}$ and $\hat{\omega}$, can be computed by Equation (13); the erroneous value is defined by

$$\hat{\hat{\theta}}_w = f_{\theta_w}(D_1, D_2, \hat{R}, \hat{\omega})$$

where $\hat{\hat{\theta}}_w$ is used in distinction to $\hat{\theta}_w$ because $\hat{\hat{\theta}}_w$ contains an error propagated from $\hat{R}$ and $\hat{\omega}$ whose errors were originally introduced by $\hat{D}_1$. In contrast, $\hat{\theta}_w$ is erroneous due to the error in $\hat{D}_1$, directly and exclusively.

Similarly, for computing the distance $\hat{H}_1$ to the target range, Equation (12) is used, and parameter dependency is as $\hat{H}_1 = f_{H_1}(D_1, \hat{R}, \hat{\omega})$.

$\frac{\varepsilon_{D_1}}{D_1}$(%)	$\hat{D}_1$	$\hat{R}$	$\frac{\varepsilon_R}{R}$(%)	$\hat{\omega}$	$\frac{\varepsilon_\omega}{\omega}$(%)	$\hat{d}_w$	$\frac{\varepsilon_d}{d_w}$(%)	$\hat{V}_1$	$\frac{\varepsilon_{V_1}}{V_1}$(%)
-10	0.90	0.3356	34.28	157.21	7.03	60.0	-14.35	2.1755	8.41
-8	0.92	0.3178	27.14	155.60	5.94	61.9	-11.59	2.1417	6.73
-6	0.94	0.3002	20.11	153.80	4.71	63.9	-8.78	2.1079	5.05
-4	0.96	0.2830	13.23	151.77	3.33	65.9	-5.91	2.0742	3.36
-2	0.98	0.2662	6.52	149.48	1.77	67.9	-2.98	2.0404	1.68
0	1.00	0.2499	0.00	146.88	0.00	70.0	0.00	2.0067	0.00
2	1.02	0.2343	-6.27	143.92	-2.01	72.1	3.05	1.9729	-1.68
4	1.04	0.2193	-12.25	140.55	-4.31	74.3	6.15	1.9391	-3.36
6	1.06	0.2053	-17.87	136.69	-6.94	76.5	9.33	1.9054	-5.05
8	1.08	0.1923	-23.06	132.28	-9.94	78.8	12.56	1.8716	-6.73
10	1.10	0.1807	-27.72	127.27	-13.35	81.1	15.87	1.8378	-8.41

Example (1)

$\frac{\varepsilon_{D_1}}{D_1}$(%)	$\hat{D}_1$	$\hat{R}$	$\frac{\varepsilon_R}{R}$(%)	$\hat{\omega}$	$\frac{\varepsilon_\omega}{\omega}$(%)	$\hat{d}_w$	$\frac{\varepsilon_d}{d_w}$(%)	$\hat{V}_1$	$\frac{\varepsilon_{V_1}}{V_1}$(%)
-10	3.60	0.8066	38.85	141.90	24.56	59.0	-15.69	7.6984	9.61
-8	3.68	0.7496	29.04	137.74	20.91	61.1	-12.71	7.5635	7.69
-6	3.76	0.6973	20.04	132.93	16.69	63.2	-9.65	7.4286	5.76
-4	3.84	0.6509	12.04	127.38	11.81	65.4	-6.52	7.2936	3.84
-2	3.92	0.6116	5.28	121.04	6.25	67.7	-3.30	7.1587	1.92
0	4.00	0.5809	0.00	113.92	0.00	70.0	0.00	7.0237	0.00
2	4.08	0.5603	-3.55	106.14	-6.83	72.4	3.39	6.8887	-1.92
4	4.16	0.5509	-5.17	97.94	-14.03	74.8	6.88	6.7537	-3.84
6	4.24	0.5532	-4.77	89.62	-21.33	77.3	10.46	6.6187	-5.77
8	4.32	0.5671	-2.38	81.55	-28.41	79.9	14.15	6.4836	-7.69
10	4.40	0.5918	1.88	74.02	-35.02	82.6	17.94	6.3486	-9.61

Example (2)

$\frac{\varepsilon_{D_1}}{D_1}$(%)	$\hat{D}_1$	$\hat{R}$	$\frac{\varepsilon_R}{R}$(%)	$\hat{\omega}$	$\frac{\varepsilon_\omega}{\omega}$(%)	$\hat{d}_w$	$\frac{\varepsilon_d}{d_w}$(%)	$\hat{V}_1$	$\frac{\varepsilon_{V_1}}{V_1}$(%)
-10	5.40	0.4844	-28.43	104.37	133.68	62.1	-11.23	6.1018	10.95
-8	5.52	0.4705	-30.48	89.98	101.47	63.7	-9.01	5.9814	8.76
-6	5.64	0.4869	-28.05	75.68	69.44	65.3	-6.78	5.8610	6.57
-4	5.76	0.5308	-21.56	63.03	41.12	66.8	-4.53	5.7405	4.38
-2	5.88	0.5962	-11.91	52.73	18.05	68.4	-2.27	5.6202	2.19
0	6.00	0.6768	0.00	44.66	0.00	70.0	0.00	5.5000	0.00
2	6.12	0.7678	13.45	38.41	-14.00	71.6	2.28	5.3794	-2.19
4	6.24	0.8660	27.96	33.53	-24.82	73.2	4.58	5.2590	-4.38
6	6.36	0.9692	43.21	29.67	-33.58	74.8	6.89	5.1387	-6.57
8	6.48	1.0759	58.98	26.56	-40.54	76.4	9.21	5.0183	-8.75
10	6.60	1.1852	75.13	24.02	-46.23	78.1	11.54	4.8980	-10.94

Example (3)

$\frac{\varepsilon_{D_1}}{D_1}$(%)	$\hat{D}_1$	$\hat{R}$	$\frac{\varepsilon_R}{R}$(%)	$\hat{\omega}$	$\frac{\varepsilon_\omega}{\omega}$(%)	$\hat{d}_w$	$\frac{\varepsilon_d}{d_w}$(%)	$\hat{V}_1$	$\frac{\varepsilon_{V_1}}{V_1}$(%)
-10	18.0	2.6674	57.57	141.17	52.73	62.3	-11.01	22.008	10.04
-8	18.4	2.3708	40.05	135.01	46.06	63.8	-8.83	21.606	8.03
-6	18.8	2.1092	24.59	127.21	37.62	65.4	-6.64	21.205	6.02
-4	19.2	1.8971	12.07	117.44	27.05	66.9	-4.43	20.803	4.01
-2	19.6	1.7525	3.53	105.66	14.31	68.4	-2.22	20.402	2.01
0	20.0	1.6928	0.00	92.43	0.00	70.0	0.00	20.000	0.00
2	20.4	1.7268	2.01	79.01	-14.52	71.6	2.23	19.600	-2.01
4	20.8	1.8493	9.24	66.74	-27.80	73.1	4.47	19.197	-4.01
6	21.2	2.0444	20.77	56.40	-38.98	74.7	6.73	18.796	-6.02
8	21.6	2.2937	35.49	48.08	-47.98	76.3	8.99	18.395	-8.03
10	22.0	2.5814	52.49	41.51	-55.10	77.9	11.26	17.994	-10.03

Example (4)

Table 2.2. Propagation of errors, from D_1 to $\hat{d}_w$ or $\hat{V}_1$.

Finally, we use the width $\hat{\theta}_w$ of the angular disparity interval for calculating the width $\hat{d}_w$ of the image disparity interval, and $\hat{H}_1$ for calculating $\hat{V}_1$. We have $\hat{d}_w = f_{d_w}(\hat{\theta}_w, \hat{W})$ using Equation (2), and $\hat{V}_1 = f_{V_1}(\hat{H}_1, \varphi)$ using Equation (1).

Numerical results for the described error propagation, starting with assumed errors in D_1, then at first to errors in R and ω, and second to errors in d_w and V_1, are presented in Table 2.2 using scene specification values as in Table 2.1. Errors are measured in percentage, and definitions are shown in the header of Table 2.2. The unit of $\hat{D}_1$, $\hat{R}$ and $\hat{V}_1$ is meter, $\hat{\omega}$ is given in degree, and $\hat{d}_w$ in pixel.

We consider an error interval of $[-10\%, +10\%]$ for D_1. A positive (negative) sign means that the erroneous value is greater (smaller) than the true value. The shaded middle row in each of the four tables in Table 2.2 shows error-free values for reference. With respect to absolute values, the greater ε_{D_1} the greater ε_R and ε_ω in general. Exceptions occur [e.g., the smallest value of ε_R for Example (2) appears for the considered maximum error ε_{D_1}; see row for a 10% error of ε_{D_1}]. Similarly, in Example (3) the considered minimum of ε_{D_1}(i.e., at -10%) leads (only) to a -28.43% error for ε_R which is less than the -30.48% error for ε_R caused by a -8% error for ε_{D_1}. For understanding this behavior, see investigations as reported in the next chapter.

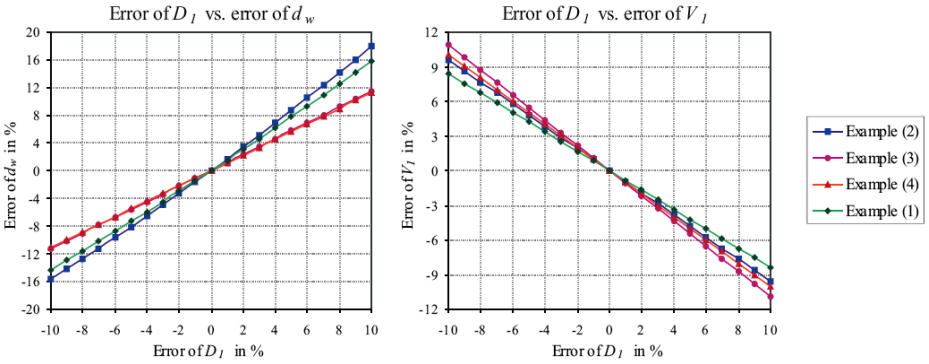

Figure 2.13. Errors of D_1 versus errors of $\hat{d}_w$ and $\hat{V}_1$.

A general interpretation of experienced experimental error propagations is as follows: errors in ε_R and ε_ω increase (in absolute values) exponentially with respect to ε_{D_1}, and the speed of increases varies for positive or negative errors, or from example to example. [See the next chapter for a more general analysis.]

Besides exponential changes in ε_R or ε_ω, errors ε_{d_w} and ε_{V_1} change with respect to ε_{D_1}(surprisingly !) approximately linearly. Figure 2.13 plots propagation results for examples (1-4) The diagram on the left shows ε_{D_1} versus ε_{d_w}. Lines for Examples (1) and (2) have steeper slopes than those for Examples (3) and (4), and this indicates that indoor acquisition might be more sensitive (with respect to ε_{d_w}) to errors in ε_{D_1}– compared to outdoor acquisition. The diagram on the right (i.e., ε_{D_1} versus ε_{V_1}) shows steeper slopes for (3) and (4) compared to (1) and (2).

Both diagrams also show opposite behavior with respect to the general trend: on the left, when ε_{D_1} is increasing then ε_{d_w} is also increasing; on the right, when ε_{D_1} is increasing then ε_{V_1} is decreasing.

In terms of magnitude, the error interval $[-10\%, +10\%]$ of D_1 introduces maximum errors of 75.13% for ε_R, and 133.68% for ε_ω, but (only) about 10% for both ε_{d_w} and ε_{V_1}. This indicates that parameters d_w and V_1 are approximately linearly affected by error ε_{D_1}.

2.4.4. ERROR IN FURTHEST SCENE RANGE

Analogously to the previous subsection, we consider now the propagation of the independent error ε_{D_2}, first to calculated parameters R and ω, and then to d_w and V_1.

Unlike parameter $\hat{D}_1$, parameter $\hat{D}_2$ does not affect the number W of image columns nor the width θ_w of the angular disparity interval at all. But

both parameters R and ω are affected, and we denote resulting erroneous values by $\hat{R}$ and $\hat{\omega}$. The corresponding errors are defined as follows:

$$\begin{aligned}\varepsilon_R &= \hat{R} - R \\ &= f_R(D_1, \hat{D}_2, H_1, \theta_w) - f_R(D_1, D_2, H_1, \theta_w)\end{aligned}$$

and

$$\begin{aligned}\varepsilon_\omega &= \hat{\omega} - \omega \\ &= f_\omega(D_1, \hat{D}_2, H_1, \theta_w) - f_\omega(D_1, D_2, H_1, \theta_w)\end{aligned}$$

The width $\hat{\theta}_w$ of the angular disparity interval, assuming the use of previously determined parameters $\hat{R}$ and $\hat{\omega}$, can be computed by Equation (13). This is abbreviated as

$$\hat{\theta}_w = f_{\theta_w}(D_1, D_2, \hat{R}, \hat{\omega})$$

Equation (12) is used for computing the distance $\hat{H}_1$ to the target range, and the parameter dependency is as $\hat{H}_1 = f_{H_1}(D_1, \hat{R}, \hat{\omega})$.

For analyzing results of error propagation, we convert the width $\hat{\theta}_w$ of the angular disparity interval into the width $\hat{d}_w$ of the image disparity interval width, and $\hat{H}_1$ into $\hat{V}_1$. We have $\hat{d}_w = f_{d_w}(\hat{\theta}_w, W)$ using Equation (2), and $\hat{V}_1 = f_{V_1}(\hat{H}_1, \varphi)$ using Equation (1).

$\frac{\varepsilon_{D_2}}{D_2}$(%)	$\hat{D}_2$	$\hat{R}$	$\frac{\varepsilon_R}{R}$(%)	$\hat{\omega}$	$\frac{\varepsilon_\omega}{\omega}$(%)	$\hat{d}_w$	$\frac{\varepsilon_d}{d_w}$(%)	$\hat{V}_1$	$\frac{\varepsilon_{V_1}}{V_1}$(%)
-10	2.70	0.2553	2.14	145.53	-0.92	74.1	5.86	2.0067	0.00
-8	2.76	0.2540	1.65	145.83	-0.72	73.2	4.53	2.0067	0.00
-6	2.82	0.2529	1.19	146.12	-0.52	72.3	3.28	2.0067	0.00
-4	2.88	0.2518	0.76	146.39	-0.34	71.5	2.12	2.0067	0.00
-2	2.94	0.2509	0.37	146.64	-0.16	70.7	1.03	2.0067	0.00
0	3.00	0.2499	0.00	146.88	0.00	70.0	0.00	2.0067	0.00
2	3.06	0.2491	-0.35	147.11	0.16	69.3	-0.97	2.0067	0.00
4	3.12	0.2483	-0.67	147.33	0.31	68.7	-1.88	2.0067	0.00
6	3.18	0.2475	-0.97	147.54	0.45	68.1	-2.74	2.0067	0.00
8	3.24	0.2468	-1.26	147.74	0.58	67.5	-3.56	2.0067	0.00
10	3.30	0.2461	-1.53	147.93	0.71	67.0	-4.33	2.0067	0.00

Example (1)

$\frac{\varepsilon_{D_2}}{D_2}$(%)	$\hat{D}_2$	$\hat{R}$	$\frac{\varepsilon_R}{R}$(%)	$\hat{\omega}$	$\frac{\varepsilon_\omega}{\omega}$(%)	$\hat{d}_w$	$\frac{\varepsilon_d}{d_w}$(%)	$\hat{V}_1$	$\frac{\varepsilon_{V_1}}{V_1}$(%)
-10	9.0	0.6217	7.02	112.85	-0.94	75.6	7.97	7.0237	0.00
-8	9.2	0.6123	5.39	113.08	-0.74	74.3	6.13	7.0237	0.00
-6	9.4	0.6035	3.89	113.30	-0.54	73.1	4.43	7.0237	0.00
-4	9.6	0.5955	2.50	113.51	-0.36	72.0	2.85	7.0237	0.00
-2	9.8	0.5879	1.21	113.72	-0.17	71.0	1.37	7.0237	0.00
0	10.0	0.5809	0.00	113.92	0.00	70.0	0.00	7.0237	0.00
2	10.2	0.5744	-1.13	114.11	0.17	69.1	-1.29	7.0237	0.00
4	10.4	0.5682	-2.18	114.30	0.33	68.3	-2.49	7.0237	0.00
6	10.6	0.5625	-3.17	114.47	0.49	67.5	-3.63	7.0237	0.00
8	10.8	0.5571	-4.11	114.65	0.64	66.7	-4.69	7.0237	0.00
10	11.0	0.5520	-4.98	114.81	0.78	66.0	-5.70	7.0237	0.00

Example (2)

$\frac{\varepsilon_{D_2}}{D_2}$(%)	$\hat{D}_2$	$\hat{R}$	$\frac{\varepsilon_R}{R}$(%)	$\hat{\omega}$	$\frac{\varepsilon_\omega}{\omega}$(%)	$\hat{d}_w$	$\frac{\varepsilon_d}{d_w}$(%)	$\hat{V}_1$	$\frac{\varepsilon_{V_1}}{V_1}$(%)
-10	45.0	0.6815	0.70	45.13	1.05	71.1	1.54	5.5000	0.00
-8	46.0	0.6804	0.55	45.03	0.82	70.8	1.20	5.5000	0.00
-6	47.0	0.6795	0.40	44.93	0.60	70.6	0.88	5.5000	0.00
-4	48.0	0.6785	0.26	44.84	0.39	70.4	0.57	5.5000	0.00
-2	49.0	0.6776	0.13	44.75	0.19	70.2	0.28	5.5000	0.00
0	50.0	0.6768	0.00	44.66	0.00	70.0	0.00	5.5000	0.00
2	51.0	0.6759	-0.12	44.58	-0.18	69.8	-0.27	5.5000	0.00
4	52.0	0.6752	-0.24	44.50	-0.36	69.6	-0.52	5.5000	0.00
6	53.0	0.6744	-0.35	44.43	-0.53	69.5	-0.77	5.5000	0.00
8	54.0	0.6737	-0.45	44.35	-0.69	69.3	-1.00	5.5000	0.00
10	55.0	0.6730	-0.55	44.28	-0.85	69.1	-1.22	5.5000	0.00

Example (3)

$\frac{\varepsilon_{D_2}}{D_2}$(%)	$\hat{D}_2$	$\hat{R}$	$\frac{\varepsilon_R}{R}$(%)	$\hat{\omega}$	$\frac{\varepsilon_\omega}{\omega}$(%)	$\hat{d}_w$	$\frac{\varepsilon_d}{d_w}$(%)	$\hat{V}_1$	$\frac{\varepsilon_{V_1}}{V_1}$(%)
-10	180.0	2.6674	1.25	92.46	0.03	70.9	1.25	20.000	0.00
-8	184.0	2.3708	0.97	92.46	0.03	70.7	0.97	20.000	0.00
-6	188.0	2.1092	0.71	92.45	0.02	70.5	0.71	20.000	0.00
-4	192.0	1.8971	0.46	92.44	0.01	70.3	0.46	20.000	0.00
-2	196.0	1.7525	0.23	92.44	0.01	70.2	0.23	20.000	0.00
0	200.0	1.6928	0.00	92.43	0.00	70.0	0.00	20.000	0.00
2	204.0	1.7268	-0.22	92.43	-0.01	69.8	-0.22	20.000	0.00
4	208.0	1.8493	-0.42	92.42	-0.01	69.7	-0.42	20.000	0.00
6	212.0	2.0444	-0.62	92.42	-0.02	69.6	-0.62	20.000	0.00
8	216.0	2.2937	-0.81	92.41	-0.02	69.4	-0.82	20.000	0.00
10	220.0	2.5814	-1.00	92.41	-0.03	69.3	-1.00	20.000	0.00

Example (4)

Table 2.3. Propagation of errors, from D_2 to $\hat{d}_w$ and $\hat{V}_1$.

For numerical data for error propagation (first of the D_2 error into errors of R and ω, and then into errors of d_w and V_1), see Table 2.3. Again we use the four scene examples as in Table 2.1. All the errors are measured in percentage, and definitions are shown in the header of Table 2.3. The unit of $\hat{D}_2$, $\hat{R}$ and $\hat{V}_1$ is meter, $\hat{\omega}$ is in degree, and $\hat{d}_w$ in pixel. We provide data for the error interval $[-10\%, +10\%]$ for D_2. A positive (negative) sign means the value is greater (smaller) than the true value. Shaded middle rows of the four tables show error-free values for reference.

The greater the magnitude of ε_{D_2} the greater the magnitudes of ε_R, ε_ω and ε_{d_w}, in all four cases. Although the errors change exponentially, the quantities are in fact considerably small for the interval $[-10\%, +10\%]$ in comparison to those for ε_{D_1}. The maximum errors of ε_R, ε_ω and ε_{d_w} are 7.02%, 1.05% and 7.97%, while they had been 75.13%, 133.68% and 17.94% for ε_{D_1}.

Figure 2.14 shows steeper slopes in curves for Examples (1) and (2) compared to those for Examples (3) and (4); this indicates that ε_{d_w} might be more sensitive to ε_{D_2} for indoor acquisition than for outdoor cases. Moreover, in general, change rates of ε_R, ε_ω and ε_{d_w} with respect to the change of ε_{D_2} are larger for negative errors than for positive errors. Note that for the indoor case, the worst case is about 7.97% ε_{d_w} for the interval $[-10\%, +10\%]$ of ε_{D_2}; but for the outdoor cases, the worst case is about 1.54% ε_{d_w} (i.e., about one pixel difference to the true width of the disparity interval, which only causes a minor loss in stereoacuity).

In Table 2.3 we have $\varepsilon_{V_1} = 0$, which suggests that ε_{D_2} introduces no error to V_1 at all. This result can be interpreted as follows. Since $\hat{V}_1 = f_{V_1}(\hat{H}_1, \varphi)$ and $V_1 = f_{V_1}(H_1, \varphi)$, we know that $\hat{V}_1 = V_1$ if $\hat{H}_1 = H_1$. Furthermore, $\hat{H}_1 = H_1$ if $f_{H_1}(D_1, \hat{R}, \hat{\omega}) = f_{H_1}(D_1, R, \omega)$, where f_{H_1} is defined by Equation (12).

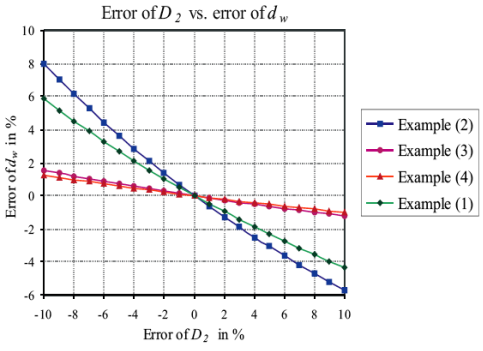

Figure 2.14. Errors of D_2 versus error of d_w.

It is very complicated to show $\hat{H}_1 = H_1$ algebraically. We can use the fact that if two circles $\hat{\mathcal{H}}$ and $\mathcal{H}$ (see Figure 2.8) with radii $\hat{H}_1$ and H_1, respectively, coincide then $\hat{H}_1 = H_1$. Since $R = f_R(D_1, D_2, H_1, \theta_w)$ and $\omega = f_\omega(D_1, D_2, H_1, \theta_w)$, $f_{H_1}(D_1, R, \omega)$ defines a circle $\mathcal{H}$ whose center is D_1 away from the center **O** of the base circle, and the radius is H_1. Furthermore, since $\hat{R} = f_R(D_1, \hat{D}_2, H_1, \theta_w)$ and $\hat{\omega} = f_\omega(D_1, \hat{D}_2, H_1, \theta_w)$, $f_{H_1}(D_1, \hat{R}, \hat{\omega})$ defines a circle $\hat{\mathcal{H}}$ whose center is D_1 away from the center **O** of the base circle, and the radius is H_1.

Both circles $\hat{\mathcal{H}}$ and $\mathcal{H}$ may coincide if both centers are at the inner circle of radius D_1, and the radiuses are equal to H_1. In this case we have $\hat{H}_1 = H_1$, and thus $\hat{V}_1 = V_1$.

To conclude, ε_{D_2} has an impact on image quality results only with respect to stereoacuity (assuming parameter specification as in Theorem 2.1).

2.4.5. DISTANCE ERROR TO TARGET RANGE

Error ε_{H_1} causes an erroneous number $\hat{W}$, and this leads to an erroneous $\hat{\theta}_w = f_{\theta_w}(d_w, \hat{W})$. Both parameters R and ω in Equations (9) and (11) depend on the four variables D_1, D_2, H_1 and θ_w. Thus, erroneous values $\hat{W}$ and $\hat{\theta}_w$ cause erroneous values $\hat{R}$ and $\hat{\omega}$, and the errors are defined, respectively, as follows:

$$\begin{aligned} \varepsilon_R &= \hat{R} - R \\ &= f_R(D_1, D_2, \hat{H}_1, \hat{\theta}_w) - f_R(D_1, D_2, H_1, \theta_w) \end{aligned}$$

and

$$\begin{aligned} \varepsilon_\omega &= \hat{\omega} - \omega \\ &= f_\omega(D_1, D_2, \hat{H}_1, \hat{\theta}_w) - f_\omega(D_1, D_2, H_1, \theta_w) \end{aligned}$$

The width $\hat{\hat{\theta}}_w$ of the angular disparity interval is now assumed to be calculated by using Equation (13), using previously calculated control values $\hat{R}$ and $\hat{\omega}$; in abbreviation, we use

$$\hat{\hat{\theta}}_w = f_{\theta_w}(D_1, D_2, \hat{R}, \hat{\omega})$$

in the error propagation experiments. Because $\hat{R} = f_R(D_1, D_2, \hat{H}_1, \hat{\theta}_w)$, $\hat{\omega} = f_\omega(D_1, D_2, \hat{H}_1, \hat{\theta}_w)$, and $\hat{\hat{\theta}}_w = f_{\theta_w}(D_1, D_2, \hat{R}, \hat{\omega})$ share the same parameters D_1, D_2, $\hat{H}_1$, $\hat{R}$, and $\hat{\omega}$, it can be shown that

$$\hat{\hat{\theta}}_w = \hat{\theta}_w$$

Equation (12) is used for computing the distance $\hat{H}_1$ between optical centers and inner cylinder of RoI. Parameter dependency is as $\hat{H}_1 = f_{H_1}(D_1, \hat{R}, \hat{\omega})$.

$\frac{\varepsilon_{H_1}}{H_1}$(%)	$\hat{H}_1$	$\hat{R}$	$\frac{\varepsilon_R}{R}$(%)	$\hat{\omega}$	$\frac{\varepsilon_\omega}{\omega}$(%)	$\hat{d}_w$	$\frac{\varepsilon_d}{d_w}$(%)	$\hat{V}_1$	$\frac{\varepsilon_{V_1}}{V_1}$(%)
-10	1.080	0.1510	-39.59	125.45	-14.59	70.0	0.00	1.8060	-10.0
-8	1.104	0.1683	-32.66	131.67	-10.36	70.0	0.00	1.8461	-8.0
-6	1.128	0.1872	-25.09	136.69	-6.94	70.0	0.00	1.8863	-6.0
-4	1.152	0.2073	-17.04	140.77	-4.16	70.0	0.00	1.9264	-4.0
-2	1.176	0.2283	-8.65	144.11	-1.89	70.0	0.00	1.9665	-2.0
0	1.200	0.2499	0.00	146.88	0.00	70.0	0.00	2.0067	0.0
2	1.224	0.2721	8.85	149.21	1.59	70.0	0.00	2.0468	2.0
4	1.248	0.2946	17.85	151.19	2.93	70.0	0.00	2.0869	4.0
6	1.272	0.3174	26.98	152.88	4.08	70.0	0.00	2.1270	6.0
8	1.296	0.3404	36.21	154.35	5.08	70.0	0.00	2.1672	8.0
10	1.320	0.3637	45.51	155.63	5.96	70.0	0.00	2.2073	10.0

Example (1)

$\frac{\varepsilon_{H_1}}{H_1}$(%)	$\hat{H}_1$	$\hat{R}$	$\frac{\varepsilon_R}{R}$(%)	$\hat{\omega}$	$\frac{\varepsilon_\omega}{\omega}$(%)	$\hat{d}_w$	$\frac{\varepsilon_d}{d_w}$(%)	$\hat{V}_1$	$\frac{\varepsilon_{V_1}}{V_1}$(%)
-10	3.78	0.5151	-11.32	68.22	-40.12	70.0	0.00	6.3213	-10.0
-8	3.86	0.5002	-13.89	77.78	-31.72	70.0	0.00	6.4618	-8.0
-6	3.95	0.4999	-13.95	87.64	-23.07	70.0	0.00	6.6023	-6.0
-4	4.03	0.5141	-11.51	97.24	-14.64	70.0	0.00	6.7428	-4.0
-2	4.12	0.5417	-6.75	106.09	-6.87	70.0	0.00	6.8832	-2.0
0	4.2	0.5809	0.00	113.92	0.00	70.0	0.00	7.0237	0.0
2	4.28	0.6295	8.37	120.65	5.91	70.0	0.00	7.1642	2.0
4	4.37	0.6855	18.01	126.36	10.92	70.0	0.00	7.3046	4.0
6	4.45	0.7473	28.64	131.17	15.14	70.0	0.00	7.4451	6.0
8	4.54	0.8135	40.04	135.22	18.69	70.0	0.00	7.5856	8.0
10	4.62	0.8832	52.03	138.64	21.70	70.0	0.00	7.7261	10.0

Example (2)

$\frac{\varepsilon_{H_1}}{H_1}$(%)	$\hat{H}_1$	$\hat{R}$	$\frac{\varepsilon_R}{R}$(%)	$\hat{\omega}$	$\frac{\varepsilon_\omega}{\omega}$(%)	$\hat{d}_w$	$\frac{\varepsilon_d}{d_w}$(%)	$\hat{V}_1$	$\frac{\varepsilon_{V_1}}{V_1}$(%)
-10	4.95	1.1200	65.50	22.48	-49.67	70.0	0.00	8.2773	-10.0
-8	5.06	1.0226	51.11	25.34	-43.26	70.0	0.00	8.4613	-8.0
-6	5.17	0.9284	37.18	28.8	-35.52	70.0	0.00	8.6452	-6.0
-4	5.28	0.8382	23.85	33.02	-26.07	70.0	0.00	8.8291	-4.0
-2	5.39	0.7536	11.36	38.22	-14.43	70.0	0.00	9.0131	-2.0
0	5.5	0.6768	0.00	44.66	0.00	70.0	0.00	9.1970	0.0
2	5.61	0.6105	-9.78	52.63	17.83	70.0	0.00	9.3810	2.0
4	5.72	0.5588	-17.43	62.29	39.47	70.0	0.00	9.5649	4.0
6	5.83	0.5258	-22.31	73.53	64.64	70.0	0.00	9.7489	6.0
8	5.94	0.5151	-23.89	85.74	91.98	70.0	0.00	9.9328	8.0
10	6.05	0.5282	-21.95	97.9	119.19	70.0	0.00	10.1167	10.0

Example (3)

$\frac{\varepsilon_{H_1}}{H_1}$(%)	$\hat{H}_1$	$\hat{R}$	$\frac{\varepsilon_R}{R}$(%)	$\hat{\omega}$	$\frac{\varepsilon_\omega}{\omega}$(%)	$\hat{d}_w$	$\frac{\varepsilon_d}{d_w}$(%)	$\hat{V}_1$	$\frac{\varepsilon_{V_1}}{V_1}$(%)
-10	18.0	2.6674	1.25	92.46	0.03	70.0	0.00	30.1010	-10.0
-8	18.4	2.3708	0.97	92.46	0.03	70.0	0.00	30.7699	-8.0
-6	18.8	2.1092	0.71	92.45	0.02	70.0	0.00	31.4388	-6.0
-4	19.2	1.8971	0.46	92.44	0.01	70.0	0.00	32.1077	-4.0
-2	19.6	1.7525	0.23	92.44	0.01	70.0	0.00	32.7766	-2.0
0	20.0	1.6928	0.00	92.43	0.00	70.0	0.00	33.4455	0.0
2	20.4	1.7268	-0.22	92.43	-0.01	70.0	0.00	34.1144	2.0
4	20.8	1.8493	-0.42	92.42	-0.01	70.0	0.00	34.7833	4.0
6	21.2	2.0444	-0.62	92.42	-0.02	70.0	0.00	35.4522	6.0
8	21.6	2.2937	-0.81	92.41	-0.02	70.0	0.00	36.1211	8.0
10	22.0	2.5814	-1.00	92.41	-0.03	70.0	0.00	36.7901	10.0

Example (4)

Table 2.4. Propagation of errors, from H_1 to $\hat{d}_w$ and $\hat{V}_1$.

We also need to convert the width $\hat{\theta}_w$ of the angular disparity interval into the width $\hat{d}_w$ of the image disparity interval, and $\hat{H}_1$ into $\hat{V}_1$. We have

$$\hat{d}_w = f_{d_w}(\hat{\theta}_w, \hat{W})$$

using Equation (2), and $\hat{V}_1 = f_{V_1}(\hat{H}_1, \varphi)$ using Equation (1).

For numerical data of error propagation (first error ε_{H_1} to errors of R and ω, and then to errors of d_w and V_1), see Table 2.4. We use the four examples of Table 2.1. As before, an error interval of $[-10\%, +10\%]$ is considered for ε_{H_1}. All the errors are measured in percentage, and definitions are shown in the headers of Table 2.4. The unit of $\hat{D}_1$, $\hat{R}$ and $\hat{V}_1$ is meter, $\hat{\omega}$ is in degree, and $\hat{d}_w$ in pixel.

The larger the magnitude of ε_{H_1}, the larger the magnitude of ε_R and ε_ω (in general). Exceptions do occur, see (e.g.) ε_R for positive or negative errors of ε_{H_1} in Examples (2) and (3). The change rates of ε_R and ε_ω with respect to ε_{H_1} are exponential, and vary (with different speed) for positive or negative errors in the four examples. (The general behavior of such parameter interactions is discussed in the next chapter.)

Although the change rates of ε_R and ε_ω are exponential, the change rates of ε_{d_w} and ε_{V_1} with respect to ε_{H_1} are surprisingly "systematic".

First, there is no impact of ε_{H_1} on d_w, that is, $\hat{d}_w = d_w$. This explains that

$$\hat{\hat{\theta}}_w = \hat{\theta}_w$$

and $\hat{W}$, as used in $\theta_w = f_{\theta_w}(d_w, W)$, is the same as used in $d_w = f_{d_w}(\theta_w, W)$. Second, the impact of ε_{H_1} on V_1 shows a constant error percentage. This can be understood based on Equation (1), which shows that the relation between V_1 and H_1 is only defined by the scale factor $2 \times \tan(\frac{\varphi}{2})$.

To conclude, based on our image quality control method, ε_{H_1} has no effect on the resultant stereoscopic panoramas with respect to stereoacuity (i.e., numbers of depth layers), but it has impact, characterized by identical source-error percentages, on other parameters of scene composition.

CAMERA ANALYSIS AND DESIGN

The previous chapter introduced four *application-specific parameters*, namely the nearest scene range D_1, the furthest scene range D_2, a (special) distance H_1 to the target range (H_1 also characterizes the vertical field of view), and the width σ_w of the angular disparity interval (σ_w specifies stereoacuity). Estimated values of these four parameters are required as inputs for the provided image quality control method which allows to calculate optimum *camera parameters* R and ω.

The control method, however, does not allow solutions for any possible quadruple of four individual input values for D_1 D_2, H_1, and σ_w. There are geometric constraints (e.g., $D_1 < D_2$) or relations between these parameters which restrict the set of possible input values. Furthermore, such constraints or relations also restrict the set of all 6-tuples $(D_1\, D_2, H_1, \sigma_w, R, \omega)$. If R is only between 0 and $20cm$, then this (eventually) results into constraints for the other five parameters.

This chapter investigates dependencies and interactions between these six parameters. To be more precise, we analyze validity ranges, inter-relationships, and characteristics of value changes for these six parameters. The aim is to study potentials with respect to camera analysis and design.

3.1. Introduction

Cameras are limited with respect to possible parameter settings. A value of $R = 1.0m$, as available to us in some experiments, can certainly not be guaranteed in general. There might be a customer expectation that R should be (say) $20cm$ at most. The question occurs, for which scenes such a camera still would allow optimum (or "near-optimum") parameter settings, and how does such a limitation of R interact with other camera or scene parameters.[1]

[1] Applications can create somehow extreme parameter settings. For example, when a line camera was placed at a window of a revolving restaurant (spinning at maximum possible speed), R was about $12m$.

We assume a family of 3D scenes which are of interest, and the different values of scene parameters define intervals. For example, assume an interval of possible distances D_1 between camera and closest scene objects, and a number of depth levels considered to be appropriate for a particular application. The question arises: what are sufficient values of off-axis distance R and principal angle ω for satisfying those demands? For an answer see the last section of this chapter.

In the past, related studies paid great attention on how the proposed imaging approach could support a chosen area of application such as stereoscopic visualization (Huang and Hung, 1998; Wei et al., 1999a; Peleg and Ben-Ezra, 1999), stereo reconstruction (Ishiguro et al., 1992; Murray, 1995; Kang and Szeliski, 1997; Huang et al., 2001c; Shum and Szeliski, 1999), or image-based rendering (Chen, 1995; McMillan and Bishop, 1995a; Kang and Desikan, 1997; Szeliski and Shum, 1997; Rademacher and Bishop, 1998; Shum and He, 1999). Regarding the design of stereo panorama cameras, these studies have been mainly focused on epipolar geometry, optics optimization, or some other realization related or practical issues (Ishiguro et al., 1992; Shum et al., 1999; Peleg et al., 2000; Huang et al., 2001b; Seitz, 2001; Werner and Pajdla, 2001). However, issues of camera analysis and design in relation to capability and controllability for scene composition and stereoacuity have not yet been dealt with in those references.

This chapter draws attention on fundamental issues of camera analysis and design with respect to the capability and controllability for scene composition and stereoacuity (over a dynamic range of 3D scenes). Such a study provides fundamentals for the understanding of acquisition geometry of stereoscopic panoramic imaging (e.g., decisions for polycentric camera positioning). The studies in this chapter are based on a more general and flexible camera model compared to previously proposed models in (Peleg and Ben-Ezra, 1999) or (Shum et al., 1999).

The first two sections in this chapter emphasize on camera analysis, while the last section focuses on camera parameter design. The first section gives a comprehensive representation of analysis results with respect to scene composition. Discussed concepts, analysis methods or steps of the first section may be reused in the second section where we give a more focused analysis for stereoacuity.

3.2. Scene Composition Analysis

Our interest is directed on six parameters in total. If any four of them are fixed, then the values of the other two are either uniquely defined or, in some cases, have exactly two possible solutions. For example, in the previous chapter we showed that when the values of parameters D_1, D_2,

H_1 and σ_w are specified, then the values of R and ω are always uniquely determined.

If any three of these six parameters are fixed, then the values of the other three parameters are constrained to some intervals, in order to satisfy $0 \leq R < D_1 < D_2$. More specifically, Figure 7.9 allows to conclude that if any three of the six parameters are bounded (i.e., by lower and upper bounds), then valid intervals follow for the remaining three parameters. For example, if the application-specific parameters D_1 D_2 and ω are bounded, then (only) this fact already implies that the values of parameters H_1, R, and ω have to be in particular intervals. We call such a resulting interval a *conditionally valid interval*.

By specifying bounds (i.e., *endpoints* of intervals) for any three application-specific parameters, we are able to compute the conditionally valid intervals of the remaining (forth) application-specific parameter and of both camera parameters. This allows more flexibility in image quality control.

3.2.1. SIMPLIFICATIONS, MAIN FOCUS, AND LAYOUT

Throughout this chapter, let (for simplifying formal expressions)

$$\sigma_w = \frac{\theta_w}{2}$$

be half of the width of a given angular disparity interval, satisfying $0 < \sigma_w < 90°$. Figure 3.1 demonstrates an invalid case with $\sigma_w > 90°$. Because $\sigma_w > 90°$ implies $\angle 1 < 90°$, which then implies $\angle 2 > 90°$, the value of R would always be greater than D_1 in this case. Thus we conclude that the value of σ_w has to be less than 90°.

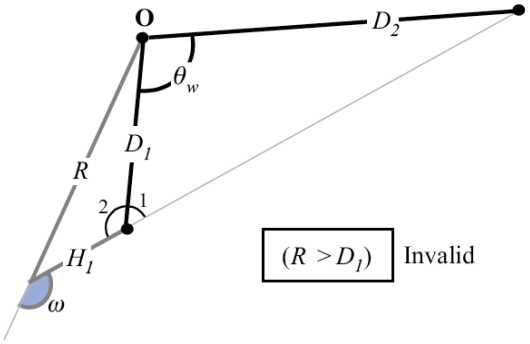

Figure 3.1. Example of an invalid case, with $\sigma_w > 90°$.

Because geometric relations between the considered six parameters are symmetric with respect to the normal vector of the base circle, we can always assume that $0° \leq \omega \leq 180°$.

In this section, we study how the camera parameters R and ω interact with the application-specific parameter H_1 while the values of the parameters D_1, D_2, and σ_w are set to be constant. We specify

- conditionally valid intervals for H_1, R, and ω,
- *mappings* characterizing convergence relations between endpoints of these three intervals, and
- the influence of value changes for one of the parameters H_1, R, or ω on values of the remaining two parameters.

For these purposes, a *geometric analysis* (i.e., a scheme for qualitative analysis) is always followed by an *algebraic analysis* (i.e., a scheme for quantitative analysis).

A geometric analysis will always proceed as follows: at first we specify preconditions of the three constants (i.e., to ensure that valid intervals exist for the three variables), then we study *interactions* (i.e., how a change of one variable influences the others) between the three variables, followed by a calculation of the conditionally valid intervals of the variables, and finally a discussion of mappings between endpoints of valid intervals of different variables.

In our algebraic analysis, we express relations between the six parameters based on both functions (for R and ω) provided earlier for image quality control. Using these functions, we derive formulas for computing endpoints as well as extrema identified before in the geometric analysis. For links between geometric and algebraic analysis, see the end of the section.

3.2.2. GEOMETRIC ANALYSIS

In the following, parameters H_1, R, and ω are variables, and D_1, D_2, and σ_w are constants, satisfying $D_1 < D_2$, and $0 < \sigma_w < 90°$.

Interaction Between Variables
When a value of one of the variables changes, then the values of the other two will change accordingly. We discuss this at first from a qualitative point of view; see Figure 3.2.

In case (A), the value of D_1 is less than the value of D_2; the value of σ_w is less than 90°; both values of R and H_1 are greater than D_1; the value of ω is greater than 90°. In the figure we use black for constant parameters and gray for variable parameters.

In case (B), a few combinations of values of H_1, R, and ω are shown for illustrating valid or invalid cases. Based on studying such combinations of values of H_1, R, and ω, we are able to conclude the following general rules:

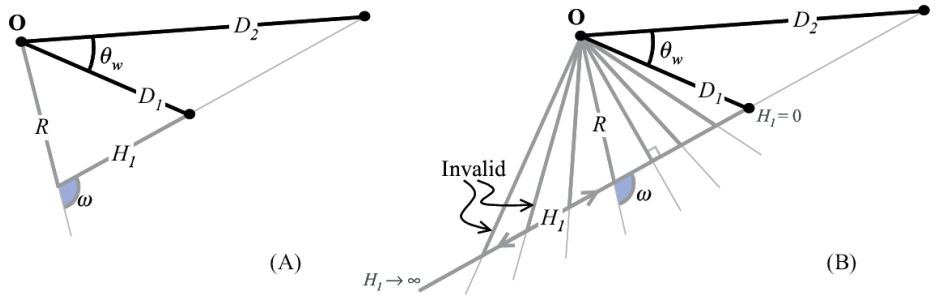

Figure 3.2. Qualitative (geometric) interaction between changes in H_1, R or ω; values of D_1, D_2, and σ_w are kept constant. (A): a simple example. (B): different states including invalid cases.

1. As H_1 increases from zero to infinity, the corresponding value of R starts at D_1, decreases first, and then increases towards infinity.

2. The value of ω increases as H_1 increases.

3. As ω increases towards 180°, the value of R starts at D_1, decreases first to $\omega = 90°$, and then increases towards infinity.

(Figure 3.2 also illustrates the calculation of endpoints of conditionally valid intervals of H_1, R, and ω; see below.)

These results also explain a phenomenon discovered within the error analysis for H_1 in the previous chapter. We recall Example (2) in Table 2.4. We noticed in this case that, while the error of H_1 increases, the determined value $\hat{R}$ of R is decreasing, regardless of the sign of the error. For a similar phenomenon, see Example (3) in this table.

Both phenomena occur because the true value of H_1 is very close to H_{1minR} such that the error interval $[-10\%, +10\%]$ of ε_{H_1} contains the value H_{1minR}. For example, the true value of H_1 is $4.2m$, which is slightly greater than H_{1minR} as $3.86m < H_{1minR} < 4.03m$. Thus, as the value of $\hat{H}_1$ decreases, the error of H_1, ε_{H_1}, increases, and the value $\hat{R}$ (estimated for R) decreases at first, namely before $\hat{H}_1 = H_{1minR}$, and increases afterwards. Therefore, when the value of ε_{H_1} increases, the value of ε_R increases at first and then starts to decrease, after the value of $\hat{H}_1$ reaches H_{1minR}.

Conditionally Valid Intervals

There are infinitely many solutions of H_1, R, and ω, for constants D_1, D_2, and σ_w and $D_1 < D_2$ and $\sigma_w < 90°$.

However, these valid values of H_1, R, and ω are limited to some intervals, due to the constraint that $R < D_1$.

Therefore, values of H_1, R, and ω cannot be specified arbitrarily for image acquisition, actually only in *conditionally valid intervals*. For any value of one of the three variables in its conditionally valid interval, there exist corresponding values of the other two variables within their conditionally valid intervals. (Below we identify endpoints of conditionally valid intervals of all three variables.)

Endpoints of the conditionally valid interval of H_1
For H_1 we can initially assume any non-zero positive real. For inferring endpoints of a conditionally valid interval of H_1. see Figure 3.2(B).

First, we have that $\lim_{H_1 \to 0^+} R = D_1$ and $\lim_{H_1 \to \infty} R = \infty$: as the value of H_1 increases from zero to infinity, the corresponding value of R starts at D_1, decreases first, and then increases towards infinity. We also have the constraint $R < D_1$. Therefore, there exists a conditional maximum value of H_1 denoted as H_{1+}, and the conditionally valid interval of H_1 becomes $(0, H_{1+})$.

Endpoints of the conditionally valid interval of R
The upper endpoint of the conditionally valid interval of R is equal to D_1. Figure 3.2(B) also shows that there exists a minimum value $R_{min} > 0$ of R. The conditionally valid interval of R is $[R_{min}, D_1)$.

Endpoints of the conditionally valid interval of ω
We already have that $0 < \omega < 180°$. Figure 3.2(B) also shows that $0° < \lim_{H_1 \to 0^+} \omega < 180°$ and $\lim_{H_1 \to \infty} \omega = 180°$. From previous conclusions we also know that ω increases if H_1 increases. Thus, ω is always in the allowed range for any finite value of H_1. Because there exists a maximum value of H_1, there also exists an upper endpoint ω_+ of the conditionally valid interval of ω. Moreover, we know that when the value of H_1 goes to zero, the limit of ω equals to a minimum ω_{min}. Thus, the conditionally valid interval of ω is equal to (ω_{min}, ω_+).

Mapping of Endpoints
We discuss all three pairs of two (out of the three) variables. Mappings specify convergence relations.

Off-axis distance R and distance H_1 to target range
When H_1 is in its conditionally valid interval, the corresponding value of R is always less than the constant D_1. When the value of H_1 increases from zero to H_{1+}, the corresponding value of R starts at constant D_1, decreases until it reaches a minimum at R_{min}, and then increases towards constant

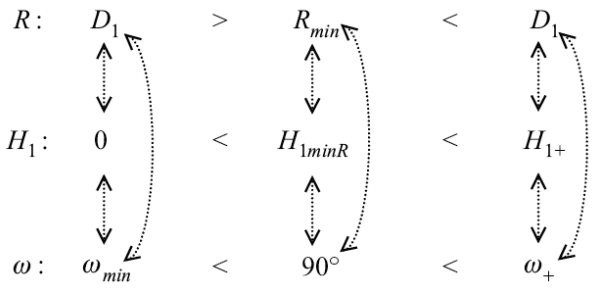

Table 3.1. Sketch of endpoint-value mappings and relations between H_1 R, and ω.

D_1. Therefore we have the following mappings of endpoints:

$$\lim_{H_1 \to 0^+} R = \lim_{H_1 \to H_{1+}} R = D_1$$

Note that these mappings are also invertible (i.e., $\lim_{R \to D_1^-} H_1 = 0$ or $= H_{1+}$). For the minimum R_{min}, there exists a corresponding value of H_1, denoted by H_{1minR}, such that

$$\lim_{H_1 \to H_{1minR}} R = R_{min}$$

The inverse relation is also true (i.e., $\lim_{R \to R_{min}} H_1 = H_{1minR}$).

These mappings are summarized in the two top rows of Table 3.1, based on the following interpretations: The variable is shown on the left, followed (right of the colon) by its endpoints and/or extrema. Symbols "<" or ">" between endpoints and/or extrema have obvious meanings. Dotted bidirectional arrows between rows (three in each column) symbolize direct dependencies. For example, the topmost arrow in the first column stands for 'when the value of R goes to D_1 then the value of H_1 goes to zero, and vise versa'.

In practice, conditionally valid intervals of the three variables normally have to be reduced due to existing conditions (imposed by camera, 3D scene geometry, and so forth). Studies of interactions between the three variables (within their conditionally valid intervals) provide information on how a change of a conditionally valid interval for one variable affects the interval of the other two. For example, if the upper bound for R needs to be reduced (e.g., for system-stabilization reasons), then it follows that both boundaries of the conditionally valid intervals of H_1 and ω need to be altered in a well-defined way (for formulas see below).

Principal angle ω and distance to target range H_1
The conditionally valid interval of ω is (ω_{min}, ω_+). The conditionally valid interval of H_1 is $(0, H_{1+})$. We already know that the value of ω increases as the value of H_1 increases, which implies that

$$\lim_{H_1 \to 0^+} \omega = \omega_{min} \quad \text{and} \quad \lim_{H_1 \to H_{1+}} \omega = \omega_+$$

If $H_1 = H_{1minR}$, then $\omega = 90°$. This is not obvious just by considering the relation between H_1 and ω, and it will be explained below when we look at the endpoint mapping between R and ω.

Note that ω_{min} is always greater than zero and less than 90°: the value of ω would be equal to zero if and only if the value of σ_w is also equal to zero, thus $\sigma_w = 0$ and there would be no stereo effect at all; on the other hand, because of $D_1 < D_2$ it follows that $\omega_{min} < 90°$.

Figure 3.2(B) indicates that $\omega_+ > 90°$ and $\omega_{min} + \omega_+ = 180°$. A proof follows in the algebraic analysis section.

Endpoint mappings for H_1 and ω are illustrated by the second and third row of Table 3.1.

Off-axis distance R and principal angle ω
The conditionally valid interval of R is $[R_{min}, D_1)$, and the conditionally valid interval of ω is (ω_{min}, ω_+). If ω increases from ω_{min} to ω_+, then R starts at D_1, decreases first until $\omega = 90°$, and then increases again towards D_1. This is in accorance with our previous conclusion that $0° < \omega_{min} < 90° < \omega_+$. It implies that

$$\lim_{\omega \to \omega_{min}^+} R = \lim_{\omega \to \omega_+^-} R = D_1$$

Figure 3.2(B) illustrates that R reaches its minimum when $\omega = 90°$. Table 3.1 summarizes the results.

We return to the question raised previously: what is the corresponding value of ω, when $H_1 = H_{1minR}$? The answer can be obtained as follows: because $H_1 = H_{1minR}$ when $R = R_{min}$, and $R = R_{min}$ when $\omega = 90°$, we can conclude that $\lim_{H_1 \to H_{1minR}} \omega = 90°$.

3.2.3. ALGEBRAIC ANALYSIS

This subsection specifies algebraic representations of previously introduced geometric relations. Two basic functions are given first, followed by derivations of formulas that allow to compute endpoints and extrema.

Basic Function
We use both functions for R and ω as derived for image quality control, but consider only H_1 as a variable. We denote these unary functions as $f_R$and f_ω, and have (in direct consequence of the general control functions):

$$f_R(H_1) = \sqrt{D_1^2 + H_1^2 + 2D_1H_1\frac{D_1 - D_2\cos\sigma_w}{\sqrt{D_1^2 + D_2^2 - 2D_1D_2\cos\sigma_w}}} \tag{1}$$

$$f_\omega(H_1) = \arccos\left(\frac{D_1D_2\cos\sigma_w - D_1^2 - H_1\sqrt{A}}{\sqrt{A(D_1^2 + H_1^2) + 2D_1H_1(D_1 - D_2\cos\sigma_w)\sqrt{A}}}\right) \tag{2}$$

where $A = D_1^2 + D_2^2 - 2D_1D_2\cos\sigma_w$.

Endpoints of Intervals and Extreme Variables
We identified endpoints or extrema R_{min}, H_{1minR}, H_{1+}, ω_{min}, and ω_+. Now we provide formulas for those (in terms of the constant parameters D_1, D_2, and σ_w).

R_{min} and H_{1minR}
The minimum value R_{min} of R and the corresponding value H_{1minR} of H_1 can be found by setting the first derivative $f'_R(H_1)$ equal to zero, and solving it with respect to H_1.

Due to a rather complicated differentiation of the function $f_R(H_1)$, we choose to differentiate instead the function of R^2, denoted as $f_{R^2}(H_1)$. This also allows to arrive at the intended minima characterization of function $f_R(H_1)$. We have

$$f_{R^2}(H_1) = D_1^2 + H_1^2 + 2D_1H_1\frac{D_1 - D_2\cos\sigma_w}{\sqrt{D_1^2 + D_2^2 - 2D_1D_2\cos\sigma_w}}$$

Thus, it follows that

$$\begin{aligned}\frac{df_{R^2}}{dH_1} &= 2H_1 + 2D_1\frac{(D_1 - D_2\cos\sigma_w)}{\sqrt{D_1^2 + D_2^2 - 2D_1D_2\cos\sigma_w}} \\ &= \frac{2\left(H_1\sqrt{D_1^2 + D_2^2 - 2D_1D_2\cos\sigma_w} + D_1(D_1 - D_2\cos\sigma_w)\right)}{\sqrt{D_1^2 + D_2^2 - 2D_1D_2\cos\sigma_w}}\end{aligned} \tag{3}$$

We set Equation (3) equal to zero and solve it with respect to H_1. We obtain

$$H_{1minR} = \frac{D_1(D_2\cos\sigma_w - D_1)}{\sqrt{D_1^2 + D_2^2 - 2D_1D_2\cos\sigma_w}} \tag{4}$$

When $H_1 = H_{1minR}$, the value of $f_R(H_1)$ is a minimum of function f_R, that is $R = R_{min}$. The value of R_{min} can be obtained from Equation (1) by substituting H_1 by the value of H_{1minR} in (4). We obtain the following:

$$\begin{aligned} R_{min} &= \sqrt{D_1^2 + \frac{D_1^2(D_1 - D_2\cos\sigma_w)^2}{D_1^2 + D_2^2 - 2D_1D_2\cos\sigma_w} - \frac{2D_1^2(D_1 - D_2\cos\sigma_w)^2}{D_1^2 + D_2^2 - 2D_1D_2\cos\sigma_w}} \\ &= D_1\sqrt{\frac{D_1^2 + D_2^2 - 2D_1D_2\cos\sigma_w - (D_1^2 + D_2^2\cos^2\sigma_w - 2D_1D_2\cos\sigma_w)}{D_1^2 + D_2^2 - 2D_1D_2\cos\sigma_w}} \\ &= \frac{D_1D_2\sin\sigma_w}{\sqrt{D_1^2 + D_2^2 - 2D_1D_2\cos\sigma_w}} \end{aligned}$$

ω_{min}

The minimum value ω_{min} of ω is equal to the limit of the values of function $f_\omega(H_1)$ as H_1 approaches to zero. It can be calculated from Equation (2) by setting $H_1 = 0$. We have

$$\begin{aligned} \omega_{min} &= \lim_{H_1 \to 0^+} f_\omega(H_1) \\ &= \arccos\left(\frac{D_1D_2\cos\sigma_w - D_1^2}{\sqrt{(D_1^2 + D_2^2 - 2D_1D_2\cos\sigma_w)D_1^2}}\right) \\ &= \arccos\left(\frac{D_2\cos\sigma_w - D_1}{\sqrt{D_1^2 + D_2^2 - 2D_1D_2\cos\sigma_w}}\right) \end{aligned}$$

H_{1+}

A previous conclusion discussed based on Table 3.1 says that the upper bound H_{1+} of H_1 can be found by setting the value of R equal to the value of D_1, which is equivalent to considering $f_R(H_1) = D_1$ and solving it for H_1. We have the following three formulas in logical consequence, step by step:

$$\begin{aligned} D_1^2 + H_1^2 + 2D_1H_1\frac{D_1 - D_2\cos\sigma_w}{\sqrt{D_1^2+D_2^2-2D_1D_2\cos\sigma_w}} &= D_1^2 \\ H_1\left(H_1 + \frac{2D_1(D_1 - D_2\cos\sigma_w)}{\sqrt{D_1^2+D_2^2-2D_1D_2\cos\sigma_w}}\right) &= 0 \\ H_1 = 0 \quad \text{or} \quad H_1 = \frac{2D_1(D_2\cos\sigma_w - D_1)}{\sqrt{D_1^2+D_2^2-2D_1D_2\cos\sigma_w}} & \end{aligned}$$

Obviously, this only allows that

$$H_{1+} = \frac{2D_1(D_2\cos\sigma_w - D_1)}{\sqrt{D_1^2 + D_2^2 - 2D_1D_2\cos\sigma_w}} \tag{5}$$

From Equations (4) and (5) we can conclude that $H_{1+} = 2H_{1minR}$.

ω_+
The upper bound ω_+ of ω can be found by substituting in Equation (2) H_1 by H_{1+} . We obtain

$$\begin{aligned}\omega_+ &= f_\omega(H_{1+}) \\ &= \arccos\left(\frac{D_1D_2\cos\sigma_w - D_1^2 - 2D_1D_2\cos\sigma_w + 2D_1^2}{\sqrt{AD_1^2 + 4D_1^2(D_2\cos\sigma_w - D_1)^2 - 4(D_1^2 - D_1D_2\cos\sigma_w)^2}}\right)\end{aligned}$$

where $A = D_1^2 + D_2^2 - 2D_1D_2\cos\sigma_w$. It follows that

$$\omega_+ = \arccos\left(\frac{D_1 - D_2\cos\sigma_w}{\sqrt{D_1^2 + D_2^2 - 2D_1D_2\cos\sigma_w}}\right) \tag{6}$$

From Equations (4) and (6) we may conclude that $\omega_+ = \pi - \omega_{min}$. This proves our previous statement that ω_{min} is complementary to ω_+ with respect to 180° (see previous analysis of the mapping of endpoints of ω and H_1, and of ω and H_1).

Validity Checking
The basic idea of a validity check is to validate any entered quadruple (D_1, D_2, H_1, σ_w) (what might be called *the user input*) whether it is acceptable for the image quality control process (i.e., leading to well-defined values of R and ω), or not.

From the last two subsections we know that we are able to obtain conditionally valid intervals of R, ω, and σ_w when values of D_1, D_2, and H_1 are specified. Similarly, we are able to obtain conditionally valid intervals of R,

	D_1	D_2	θ_w	H_{1-}	H_{1+}
(1)	1	3	10.48	0.0	1.9813
(2)	4	10	9.17	0.0	7.9292
(3)	6	50	8.00	0.0	11.9622
(4)	20	200	8.74	0.0	39.8567
H_P = 5184 (pixels)			u = 0.007 (mm)		
H_S = 768 (pixels)			f = 21.7 (mm)		

Table 3.2. Table of conditionally valid intervals of H_1 for the examples of Table 1.1 in (**?**).

ω, and H_1 when values of D_1, D_2, and σ_w are specified. These conditionally valid intervals allow a validity check on values of parameters σ_w or H_1, when the other three application-specific parameters are already known to be in specified (finitely bounded) intervals.. Table 3.2 shows as an example all conditionally valid intervals of H_1 for the four examples of Table 2.1 in (**?**).

Summary
Figure 3.3 shows the graphs of both functions $f_R(H_1)$ and $f_\omega(H_1)$. Note that they confirm the initial geometric analysis.

We summarize the curve behaviors as follows: For the graph of $f_R(H_1)$, the value of f_R starts at D_1, decreases first and then increases towards ∞ as the value of H_1 increases from 0 to ∞. For the graph of $f_\omega(H_1)$, the value of ω increases as the value of H_1 increases. In other words, the function $f_\omega(H_1)$ increases monotonically on G_{H_1}. Note that $\omega = 180°$ is the horizontal asymptote of the curve $\omega = f_\omega(H_1)$.

Although the graphs are provided for one particular combination of specified constants, their asymptotic or extreme value behavior remains basically the same for all valid values of the constant parameters (basically it only differs by scaling factors). Note that the graphs in Figure 3.3 allow us to see how a change in the values of R or ω will impact the value of H_1, because basic relations or general changing behavior do not alter. Note that there is no unique inverse function for $f_R(H_1)$.

The endpoints of the conditionally valid intervals of the three variables are also illustrated by both graphs in Figure 3.3. The conditionally valid interval $[R_{min}, D_1)$ of R, and the conditionally valid interval $(0, H_{1+})$ of H_1

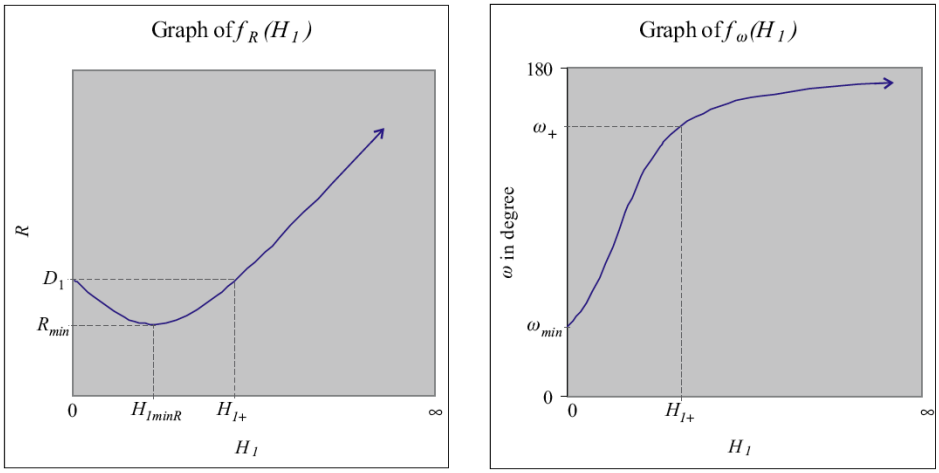

Figure 3.3. Graphs of functions $f_R(H_1)$ and $f_\omega(H_1)$.

are indicated along the axes of the graph of f_R. For the graph of f_ω, the conditionally valid interval of ω is (ω_{min}, ω_+)

Mappings between endpoint values of these intervals are represented by dashed lines, namely for the mapping between H_{1+} and D_1, and between H_{1minR} and R_{min} (in the graph of $f_R(H_1)$), and for the mapping between H_{1+} and ω_+ (in the graph of $f_R(H_1)$). These mappings are (summarized) as follows:

$$\begin{aligned} \lim_{H_1 \to 0^+} R &= \lim_{H_1 \to H_{1+}} R = D_1 \\ \lim_{H_1 \to H_{1minR}} R &= R_{min} \\ \lim_{H_1 \to 0^+} \omega &= \omega_{min} \\ \lim_{H_1 \to H_{1+}} \omega &= \omega_+ \end{aligned}$$

From these mappings and a previous conclusion drawn in the algebraic analysis subsection, we know that

$$\lim_{H_1 \to 0^+} R = \lim_{H_1 \to H_{1+}} R = D_1$$

and $H_{1+} = 2H_{1minR}$. Together with Figure 3.3 we can conclude that the curve of function $f_R(H_1)$ on the conditionally valid interval $(0, H_{1+})$ of H_1 is symmetric with respect to the straight line $H_1 = H_{1minR}$. Moreover, from the graph of function $f_\omega(H_1)$ we see that $\omega_{min} = \pi - \omega_+$, which has been obtained already previously when computing ω_+.

3.3. Stereoacuity Analysis

This section studies how camera parameters R and ω interact with the stereoacuity parameter σ_w while D_1, D_2, and H_1 are constant. In analogy to the previous case, we focus on

- conditionally valid intervals for σ_w, R, and ω under the condition of constant values for the other three parameters,
- mappings between endpoints of these intervals, and
- the influence of changes for either σ_w, R, or ω onto the values of the other two parameters.

The overall structure of the section is similar to that of the previous section.

3.3.1. GEOMETRIC ANALYSIS

As in the section before, we start with a qualitative geometric analysis, followed in the next subsection by an algebraic analysis.

Geometric model
Qualitatively there are five different possibilities to specify H_1: we may take $H_1 < D_1$, $H_1 = D_1$, $D_1 < H_1 < D_2$, $H_1 = D_2$, or $H_1 > D_2$. It turns out that the cases $H_1 \leq D_1$ and $H_1 > D_1$ are of particular interest, and we discuss both in detail. Geometries of both cases are shown in Figure 3.4 (A) and (B).

The left of Figure 3.4 (A) or (B) represents the three constant parameters by three line segments of lengths D_1, D_2 and H_1. The circular dotted arc (with center at **O**) has radius of D_1. It is used as a constraint for possible positions of focal points at distance H_1. The right of Figure 3.4 (A) or (B) illustrates the specification of variables by representing in both cases a valid combination of σ_w, R, and ω. Note that the angle σ_w between both line segments related to D_1, D_2 has to be less than 90° (as shown above).

Based on the chosen values of H_1, D_1, and D_2 in Figure 3.4 (A) and (B), Figure 3.5 (A) and (B) illustrates a few more supporting combinations of values of σ_w, R, and ω, to be used below.

Interaction Between Variables
Parameter σ_w is measured in degree. It is constrained to be less than 90°, and we do not consider $\sigma_w = 0°$ or $\sigma_w = 90°$.

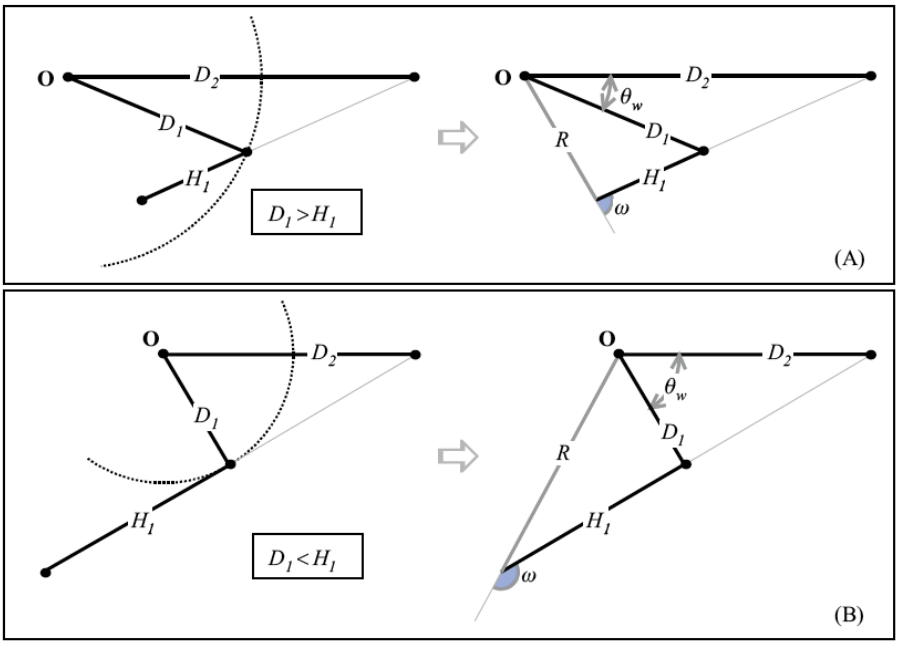

Figure 3.4. Formation of graphs for the analysis of σ_w, R, and ω.

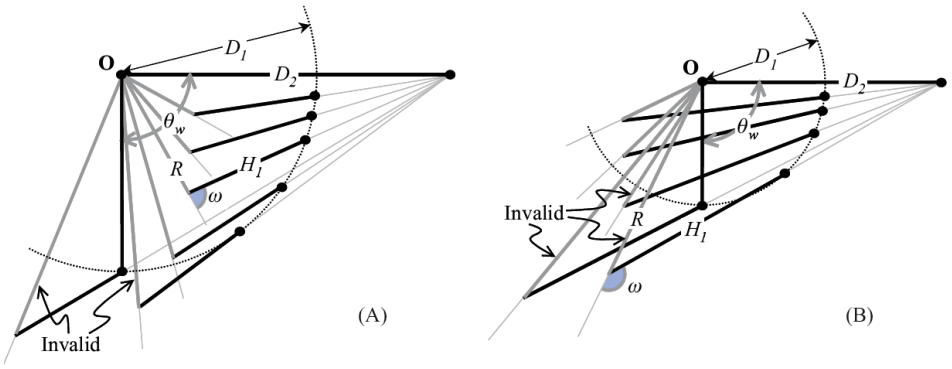

Figure 3.5. Geometry of changes in σ_w, R and ω when D_1, H_1, and H_1 are kept constant. (A): $D_1 \geq H_1$. (B): $D_1 < H_1$.

Qualitative results on variable's interactions can be obtained by geometric reasoning based on Figure 3.5 (A) and (B). We summarize qualitative results for $D_1 \geq H_1$, or $D_1 < H_1$. For case (A) we have the following:

1. R increases if σ_w increases.

2. ω increases if σ_w increases.

3. ω increases if R increases.

We have the following conclusions for case (B):

1. R increases if σ_w increases.

2. σ_w increases from $0°$ to $90°$; the value of ω starts at $180°$, decrease first, and then increases again if σ_w goes to $90°$.

3. If R increases, then ω starts at $180°$, decreases first, and then increases towards $180°$.

Conditionally Valid Intervals
The values of σ_w, R, and ω cannot be specified arbitrarily in image acquisition due to given limitations (e.g., type of camera), and we also have the constraint that $R < D_1$. This subsection analyzes the endpoints of the conditionally valid intervals for the three variables σ_w, R, ω.

Endpoints of the conditionally valid interval of σ_w
The value of σ_w is a real in the open interval $(0, 90°)$. For a geometric analysis of case $D_1 \geq H_1$, see Figure 3.5 (A).

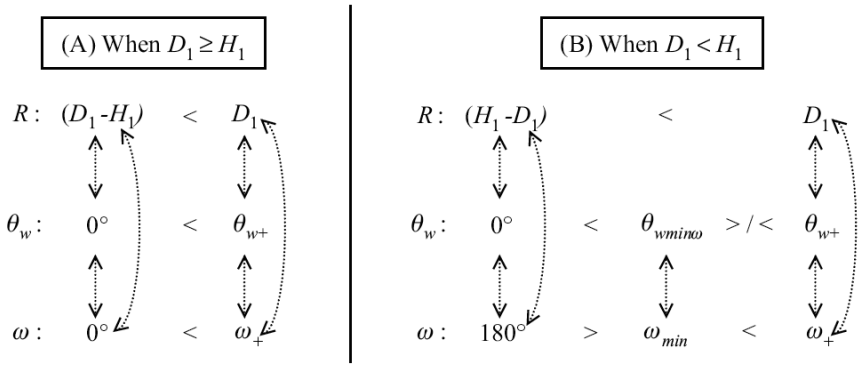

Table 3.3. Endpoint-value mappings, and relations between σ_w R, and ω.

We know that R increases if σ_w increases. We also know that

$$\lim_{\sigma_w \to 0^+} R = (D_1 - H_1)$$

and $R > D_1$ if σ_w goes to 90°. Thus, there is an upper bound σ_{w+} for σ_w, such that for any value of σ_w within the interval $(0, \sigma_{w+})$, the corresponding value of R is less than D_1. As a result, $(0, \sigma_{w+})$ is the conditionally valid interval for σ_w.

For a geometric analysis of case $D_1 < H_1$, see Figure 3.5(B). The value of R increases if σ_w increases. All the statements and results obtained for case (A) also apply for (B) except that

$$\lim_{\sigma_w \to 0^+} R = (H_1 - D_1)$$

A summary of these qualitative results (for both cases) is given in the top two rows of Table 3.3 (A) and (B).

Endpoints of the conditionally valid interval of R
The off-axis distance R is a non-negative real number with D_1 as an upper bound.

For $D_1 \geq H_1$ [see Figure 3.5 (A)], it follows that $R > D_1 - H_1$, which defines a lower bound. The conditionally valid interval of R is $(D_1 - H_1, D_1)$ in case (A).

For $D_1 < H_1$ [see Figure 3.5 (B)], we observe that $R > H_1 - D_1$), which defines a lower bound. The conditionally valid interval of R is $(H_1 - D_1, D_1)$ in case (B).

Endpoints of the conditionally valid interval of ω
The principal angle ω is a positive real less than 360°; due to symmetry of left and right camera, we only need to consider values of ω less than 180°.

The value of ω increases if σ_w increases. Thus, there exists a maximum value of σ_w in case (A), defining an upper bound ω_+ of the conditionally valid interval of ω. Figure 3.5 (A) shows that the limit of ω equals to zero as the value of σ_w goes to zero. Therefore, the conditionally valid interval of ω is $(0°, \omega_+)$ in case (A).

Consider that a change in values of ω starts at 180°, decreases first, and then increases towards 180° as the value of σ_w increases. It follows that there exists a minimum ω_{min} of ω for case (B). For case (B), $(\omega_{min}, 180°)$ is a conditionally valid interval of ω. This interval will further shrink if the value of σ_w reaches the upper bound of σ_{w+} before the value of ω reaches the minimum ω_{min}. The conditionally valid interval of ω becomes $(\omega_+, 180°)$ for this special case of (B).

Mapping of Endpoints
Now we examine mappings between endpoints of conditionally valid intervals (three different pairings of parameters).

Off-axis distance R and angular disparity width σ_w
For $D_1 \geq H_1$ [case (A)], we identified the conditionally valid interval of R as $(D_1 - H_1, D_1)$, and the conditionally valid interval of σ_w as $(0, \sigma_{w+})$. The value of R increases if σ_w increases. We have the following results:

$$\lim_{\sigma_w \to 0^+} R = (D_1 - H_1) \quad \text{and} \quad \lim_{\sigma_w \to \sigma_{w+}^-} R = D_1$$

Both mappings are uniquely invertible.

For $D_1 < H_1$ [case (B)], the conditionally valid interval of R is $(H_1 - D_1, D_1)$, and the conditionally valid interval of σ_w is $(0, \sigma_{w+})$. The "first" resulting mapping in this case is the same as in case (A), and the "second" is as follows:

$$\lim_{\sigma_w \to 0^+} R = H_1 - D_1$$

All three mappings are visualized in the two topmost rows of Table 3.3.

Principal angle ω and angular disparity width σ_w
In case (A), the conditionally valid interval of ω is $(0°, \omega_+)$. The conditionally valid interval of σ_w is $(0, \sigma_{w+})$. The value of ω increases if σ_w increases; we have

$$\lim_{\sigma_w \to 0^+} \omega = 0° \quad \text{and} \quad \lim_{\sigma_w \to \sigma_{w+}^-} \omega = \omega_+$$

In case (B), the conditionally valid interval of ω is $(\omega_{min}, 180°)$. The conditionally valid interval of σ_w is $(0, \sigma_{w+})$. The value of σ_w increases from 0° to σ_{w+}, the value of ω starts changing from 180°, decreases first, and then increases until the value of σ_w reaches σ_{w+}. Thus,

$$\lim_{\sigma_w \to 0^+} \omega = 180° \quad \text{and} \quad \lim_{\sigma_w \to \sigma_{w+}^-} \omega = \omega_+$$

This shows that we have a minimum value ω_{min}, and that there exists a corresponding value of σ_w, denoted by $\sigma_{w min\omega}$, such that

$$\lim_{\sigma_w \to \sigma_{w min\omega}} \omega = \omega_{min}$$

It is possible that $\sigma_{w+} < \sigma_{w min\omega}$, and in this special case it follows that, if σ_w increases from 0° to σ_{w+}, then ω decreases from 180° until it approaches ω_+.

The two bottom-most rows of Table 3.3 illustrate these endpoint mappings.

Off-axis distance R and principal angle ω
For $D_1 \geq H_1$ [case (A)], the conditionally valid interval of R is equal to $(D_1 - H_1, D_1)$, and the conditionally valid interval of ω is equal to $(0°, \omega_+)$. Because ω increases if R increases, we have

$$\lim_{\omega \to 0^+} R = (D_1 - H_1) \quad \text{and} \quad \lim_{\omega \to \omega_+^-} R = D_1$$

For case (B), the resulting mappings are the same as in case (A) except that

$$\lim_{\omega \to 180^-} R = (H_1 - D_1)$$

These mappings are illustrated in the two bottom-most rows of Table 3.3.

3.3.2. ALGEBRAIC ANALYSIS

The qualitative geometric analysis for σ_w is now followed by computations of endpoints or extrema. We also discuss links between qualitative and quantitative results.

Basic Functions
Let R be defined by a unary function f_R, only dependent on variable σ_w. We have the following:

$$f_R(\sigma_w) = \sqrt{D_1^2 + H_1^2 + 2D_1 H_1 \frac{D_1 - D_2 \cos\sigma_w}{\sqrt{D_1^2 + D_2^2 - 2D_1 D_2 \cos\sigma_w}}} \qquad (7)$$

Let ω be defined by a unary function f_ω with a single independent variable R. We have the following:

$$f_\omega(R) = \arccos\left(\frac{D_1^2 - H_1^2 - R^2}{2H_1 R}\right) \tag{8}$$

We also consider ω to be defined by the composite function $g_\omega = f_\omega \circ f_R$, which is a function with a single independent variable σ_w. We obtain the following:

$$g_\omega(\sigma_w) = \arccos\left(\frac{D_1 D_2 \cos\sigma_w - D_1^2 - H_1\sqrt{A}}{\sqrt{A(D_1^2 + H_1^2) + 2D_1 H_1(D_1 - D_2\cos\sigma_w)\sqrt{A}}}\right) \tag{9}$$

where $A = D_1^2 + D_2^2 - 2D_1 D_2 \cos\sigma_w$.

Endpoints and Extrema
In our geometric analysis section we identified endpoint and extreme values of variables. They are $\sigma_{wmin\omega}$, ω_{min}, σ_{w+}, and ω_+. Now we show how to compute these values in terms of given constant parameters D_1, D_2, and H_1.

σ_{w+}
The value of σ_{w+} can be found by setting $f_R(\sigma_w) = D_1$ and then solve this with respect to σ_w. We have the following two subsequent conclusions:

$$D_1^2 + H_1^2 + 2D_1 H_1 \frac{D_1 - D_2\cos\sigma_w}{\sqrt{D_1^2 + D_2^2 - 2D_1 D_2\cos\sigma_w}} = D_1^2$$

$$H_1\sqrt{D_1^2 + D_2^2 - 2D_1 D_2\cos\sigma_w} = 2D_1 D_2\cos\sigma_w - 2D_1^2$$

Now square both sides and we have the following three subsequent conclusions:

$$H_1^2 D_1^2 + H_1^2 D_2^2 - 2D_1 D_2 H_1^2\cos\sigma_w - 4D_1^2 D_2^2\cos^2\sigma_w - 4D_1^4 + 8D_1^3 D_2\cos\sigma_w = 0$$

$$4D_1^2 D_2^2\cos^2\sigma_w + 2\left(D_1 D_2 H_1^2 - 4D_1^3 D_2\right)\cos\sigma_w + \left(4D_1^4 - H_1^2 D_1^2 - H_1^2 D_2^2\right) = 0$$

$$\cos^2\sigma_w + 2\left(\frac{D_1 D_2 H_1^2 - 4D_1^3 D_2}{4D_1^2 D_2^2}\right)\cos\sigma_w + \left(\frac{4D_1^4 - H_1^2 D_1^2 - H_1^2 D_2^2}{4D_1^2 D_2^2}\right) = 0$$

Thus, the value of $\cos\sigma_w$ can be obtained by

$$\cos\sigma_w = \frac{4D_1^2 - H_1^2}{4D_1 D_2} \pm \sqrt{\left(\frac{H_1^2 - 4D_1^2}{4D_1 D_2}\right)^2 - \left(\frac{4D_1^4 - H_1^2 D_1^2 - H_1^2 D_2^2}{4D_1^2 D_2^2}\right)}$$

$$= \frac{4D_1^2 - H_1^2}{4D_1D_2} \pm \sqrt{\frac{H_1^4 - 4H_1^2D_1^2 - 4H_1^2D_2^2}{16D_1^2D_2^2}}$$
$$= \frac{4D_1^2 - H_1^2 \pm H_1\sqrt{H_1^2 - 4D_1^2 + 4D_2^2}}{4D_1D_2}$$

Both solution of σ_w can be calculated by applying the inverse cosine, and the positive solution

$$\sigma_{w+} = \arccos\left(\frac{4D_1^2 - H_1^2 + H_1\sqrt{H_1^2 - 4D_1^2 + 4D_2^2}}{4D_1D_2}\right)$$

is valid.

ω_+
The value of ω_+ can be obtained by substituting in Equation (8) R into D_1. This results into the following:

$$\begin{aligned}\omega_+ &= f_\omega(D_1)\\ &= \arccos\left(\frac{D_1^2 - H_1^2 - D_1^2}{2H_1D_1}\right)\\ &= \arccos\left(\frac{-H_1}{2D_1}\right)\end{aligned}$$

ω_{min} and $\sigma_{wmin\omega}$
Values of $\sigma_{wmin\omega}$, and ω_{min} can be found by letting the first derivative of g'_ω be equal to zero, and solving it with respect to σ_w. Because the differentiation of function g_ω [specified in Equation (9)] is rather complicated, we decided to apply (for the experiments to be reported for Figure 3.6) mathematical software in this case to find the desired values. However, note that this is actually the only case where we refrain from driving an explicit expression for the desired value.

Summary
The graphs of functions $f_R(\sigma_w)$ and $f_\omega(\sigma_w)$ are given in Figure 3.6. The graph of $f_R(\sigma_w)$ (at the top) shows that R increases if σ_w increases, for both cases (A) and (B). The graph of $f_\omega(\sigma_w)$ (at the bottom left; for $D_1 \geq H_1$), shows that ω increases if σ_w increases.

The graph of $f_\omega(\sigma_w)$ (at the bottom right; for $D_1 < H_1$), shows that ω decreases from 180°, reaches its minimum, and then increases if σ_w increases. These results confirm our earlier conclusions drawn just from geometric interpretations using Figure 3.6.

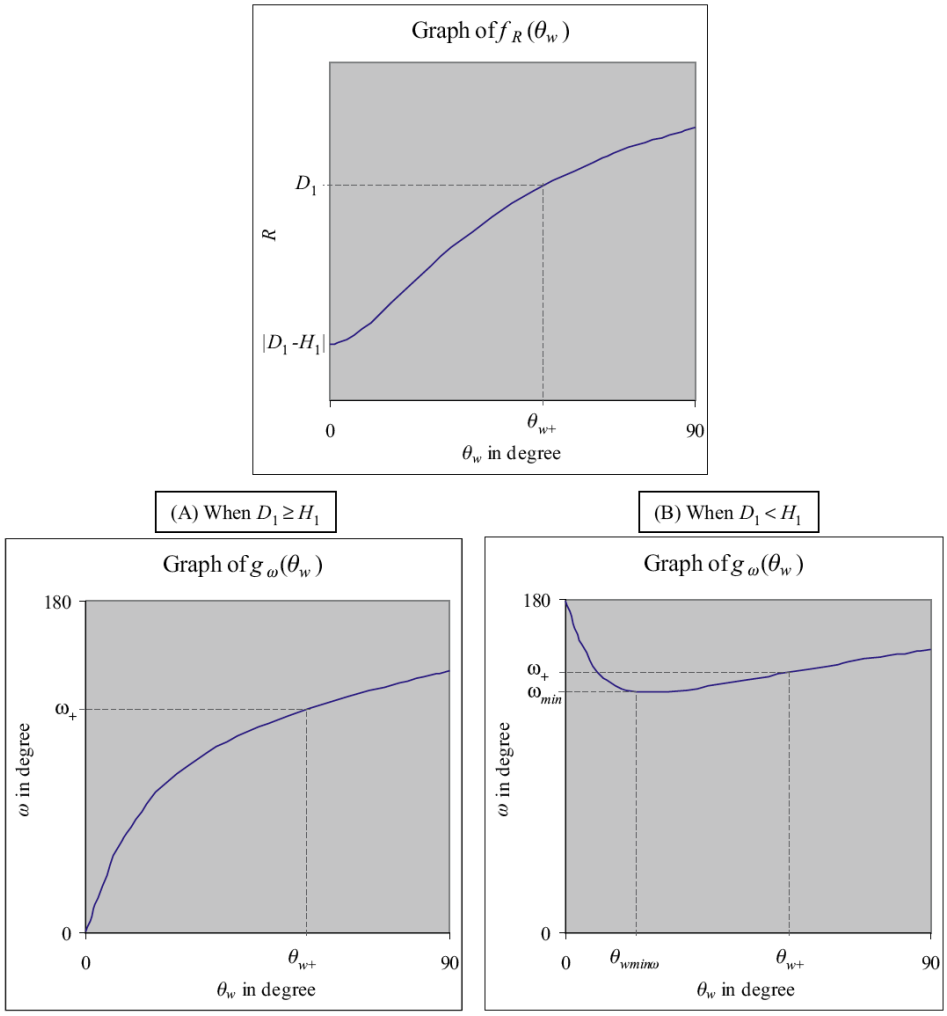

Figure 3.6. Top: graph of function $f_R(\sigma_w)$. Bottom: graphs of function $g_\omega(\sigma_w)$ for case (A) on the left, and case (B) on the right.

Although the graphs in this figure are for a particular combination of the three constants, the provided characterization is invariant to value changes (except for different scales). For the shown example of function f_ω in case (B) we have $\sigma_{wminR} < \sigma_{w+}$. In general it is also possible to have $\sigma_{wminR} = \sigma_{w+}$ or $\sigma_{wminR} > \sigma_{w+}$, depending on the three given constants. Figure 3.6 also illustrates changes in σ_w depending on changes of R or ω. Note that $f_\omega(\sigma_w)$ is not uniquely invertible for case (B).

Endpoints of the conditionally valid intervals of the three variables are

also illustrated in Figure 3.6. In the graph of f_R, the conditionally valid intervals of R and σ_w are indicated along the axes, for both cases (A) and (B). We have the conditionally valid interval $(\|D_1 - H_1\|, D_1)$ for R, and the conditionally valid interval $(0, \sigma_{w+})$ for σ_w.

The conditionally valid intervals $(0°, \omega_+)$ of ω, and $(0°, \omega_+)$ of σ_w are labeled along the axes of f_ω, for both cases (A) and (B). Additionally, the extreme ω_{min} and the corresponding value σ_{wminR} are indicated for case (B).

The following mappings between endpoints or extrema are shown in this figure by dashed lines: a mapping between σ_{w+} and D_1 in the graph of f_R, a mapping between σ_{w+} and ω_+ in the graph of f_ω [for both cases (A) and (B)], and a mapping between σ_{wminR} and ω_{min} for case (B). The mapping results may be summarized as follows:

$$\lim_{\sigma_w \to 0^+} R = |D_1 - H_1|, \quad \lim_{\sigma_w \to \sigma_{w+}^-} R = D_1, \quad \lim_{\sigma_w \to 0^+} \omega = 0°$$

for both cases,

$$\lim_{\sigma_w \to 0^+} \omega = 180°$$

for case (A), and

$$\lim_{\sigma_w \to \sigma_{w+}^-} \omega = \omega_+ \quad \text{and} \quad \lim_{\sigma_w \to \sigma_{w\,minR}} \omega = \omega_{min}$$

for case (B).

3.4. Specification of Camera Parameters

The design of stereo panorama cameras is typically concerned with epipolar geometry or optics optimization, see (Ishiguro et al., 1992; Shum et al., 1999; Peleg et al., 2000; Huang et al., 2001b; Seitz, 2001; Werner and Pajdla, 2001). This section discusses two additional criteria: controllabilities of scene composition and stereoacuity (depth levels) over dynamic ranges of 3D scenes. Lacks in these capabilities result in difficulties in camera positioning, which may increase costs, poor stereo quality such as cardboard-effects, dipopia at the time of stereo viewing, and so forth.

Parameter optimizaton is feasible after the search space for solutions is reduced based on our studies. We reduce the original (unconstrained) search space, which is a four-dimensional bounded set, to a set defined by just eight value comparisons at most. Our results can be incorporated into existing approaches (Ishiguro et al., 1992; Wei et al., 1999a; Shum et al., 1999; Peleg et al., 2000) because our camera model covers these more specific studies.

Problem Statement
The specifications of application requirements for stereo panorama image acquisition can be described by defining intervals for all four application-specific parameters. Formally we define these intervals as $[D_{1min}, D_{1max}]$, $[D_{2min}, D_{2max}]$, $[H_{1min}, H_{1max}]$, and $[\theta_{min}, \theta_{max}]$, where $D_{1max} < D_{2min}$. Values within these intervals are assumed to be valid according to our previous definition of conditionally valid intervals. In other words, for any given combination of these values within the selected intervals, there have to exist values of R and ω which satisfy the specification. Using our analysis results, the validity of the intervals can be checked beforehand, and the intervals can be adjusted if required.

In theory, the value of R can be any positive real and the value of ω can be any positive real less than 360°. Practically, considering system stabilization or cost issues, the intervals of both camera parameters should be as small as possible for an intended application.

Without loss of generality, let $R_{min} = \omega_{min} = 0$. The problem is to find minimum values of R_{max} and ω_{max} that fully satisfy specifications of the given application requirements.

3.4.1. ANALYSIS OF SCENE RANGES

Geometrically the problem consists in finding maximum values in a bounded four-dimensional space. Obviously it is difficult to imagine a hypersurface in a five-dimensional space. The applied analysis method follows our method used for parameter analysis for scene composition and stereoacuity. We will restrict our discussions on geometry and provide just summaries of analysis results.

Nearest Scene Range Analysis
We analyze interactions between $D_1 > 0$ and both camera parameters R and ω. We use $D_1 < D_2$.

Figure 3.7 illustrates the geometry of changes in D_1 versus changes R or ω, for a few values of D_2, H_1, and θ. We illustrate seven different situations of values of D_1, R, and ω. Basically we infer continuous transitions from such a finite set of states. Conclusions use just one additional precondition, namely that $\sigma_w < 90°$.

From the geometry of endpoint conditions, for parameters D_1, R and ω, we conclude the following:

(1) $\lim_{D_1 \to 0^+} R = H_1$ and $\lim_{D_1 \to 0^+} \omega = 180°$,

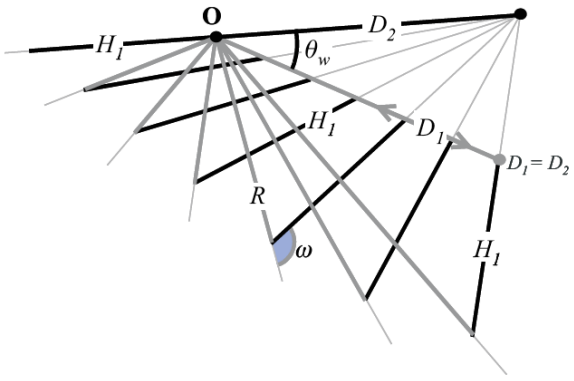

Figure 3.7. Geometry of changes in D_1, R and ω when D_2, H_1, and σ_w are assumed to be constant.

(2)

$$\lim_{D_1 \to D_2^-} R = \sqrt{D_2^2 + H_1^2 + 2D_2 H_1 \sin\left(\frac{\theta}{2}\right)}$$

and

$$\lim_{D_1 \to D_2^-} \omega = \arccos\left(\frac{-H_1 - D_2 \sin\left(\frac{\theta}{2}\right)}{\sqrt{D_2^2 + H_1^2 + 2D_2 H_1 \sin\left(\frac{\theta}{2}\right)}}\right)$$

(3) by (1) and (2), we also have that $\lim_{D_1 \to 0^+} R < \lim_{D_1 \to D_2^-} R$ and $\lim_{D_1 \to 0^+} \omega > \lim_{D_1 \to D_2^-} \omega$.

Furthermore, the geometric situation also allows to conclude that, if D_1 increases from zero to D_2, then R decreases first before increasing for all remaining increases in D_1. During such an increase in D_1, the corresponding value of ω starts at 180°, decreases first and then increases again. Thus, for $0 < D_1 < D_2$, we have the following:

(1) there exists a uniquely defined minimum of R, and
(2) there exists a uniquely defined minimum of ω.

Furthest Scene Range Analysis

We analyze interactions between D_2 and both camera parameters R and ω. D_2 is potentially any non-zero positive real greater than D_1. Figure 3.8 illustrates the geometry of changes in D_2 versus changes in R and ω [for cases (A) and (B)], while the values of D_1, H_1, and θ are kept constant. Case (A) denotes $D_1 \geq H_1$, and (B) stands for $D_1 < H_1$.

For any given values of D_1, H_1, and θ, where $\sigma_w < 90°$, we have that

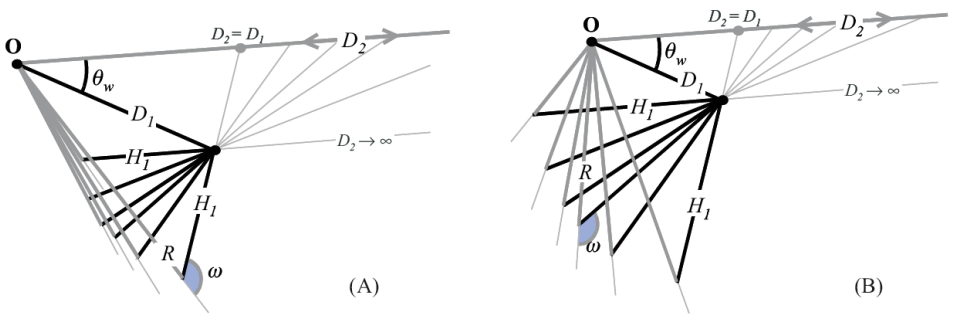

Figure 3.8. Geometry of changes in D_2, R and ω when D_1, H_1, and σ_w are kept constant. (A): $D_1 \geq H_1$. (B): $D_1 < H_1$.

(1) in both cases (A) and (B), the value of R increases (decreases) while D_2 decreases (increases);
(2) in case (A), the value of ω increases (decreases) while the value of D_2 decreases (increases);
(3) In case (B), if D_2 increases from D_1 to ∞, then ω decreases first and then increases again. There exists a minimum of ω.

This concludes the necessary information needed for specifying the camera parameters.

3.4.2. SPECIFICATION OF OFF-AXIS DISTANCE R

Figure 3.9 shows individual graphs of R with respect to any of the parameters D_1, H_1, D_2, and σ_w. All graphs illustrate for R how it changes if just one of the parameters D_1, H_1, D_2, and σ_w changes its value.

Let f_R be the function for calculating R with respect to the single variable D_1. Conclusions drawn in the previous subsection imply that function f_R is continuous, it has a single minimum, and its graph is concave (upward) on $(0, D_2)$.

Now, let f_R be the function with respect to the single variable H_1, see Equation (1). According to our results about scene composition, this function f_R is also continuous, it has a single minimum, and its graph is concave (upward) on $(0, \infty)$.

Let f_R be defined with respect to the single variable D_2. It follows that this function is continuous and decreasing on (D_1, ∞); its graph has a horizontal asymptote.

Finally, function f_R defined in Equation (7) with respect to the single variable σ_w is continuous and increasing on $(0°, 90°)$.

Because the four graphs of functions f_R, with respect to any of these four parameters, are either decreasing, increasing or concave (upward), we

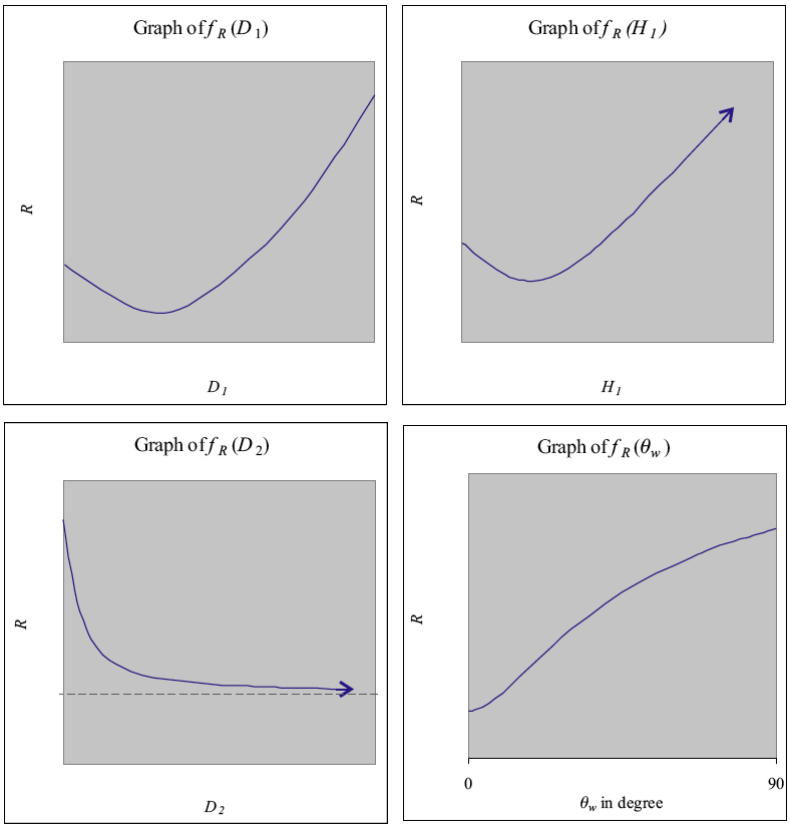

Figure 3.9. Graphs of R, in each case with respect to exactly one of the parameters D_1, D_2, H_1, or σ_w.

have that the maximum value of R within the four-dimensional hypercube, defined by the cross product of intervals $[D_{1min}, D_{1max}]$, $[D_{2min}, D_{2max}]$, $[H_{1min}, H_{1max}]$, and $[\sigma_{wmin}, \sigma_{wmax}]$, lies at one of the corners of this region. This reduces the search space for the maximum of R from a four-dimensional bounded region to 16 combinations of endpoints.

Furthermore, because function $f_R(D_2)$ is decreasing, the maximum of R is taken at $D_2 = D_{2min}$. Because $f_R(\sigma_w)$ is increasing, the maximum of R is taken at $\sigma_w = \sigma_{wmax}$. The search space is thus further reduced to four points when searching for the maximum value of R.

3.4.3. SPECIFICATION OF PRINCIPAL ANGLE ω

Figure 3.10 shows Individual function graphs for changes in ω with respect to each of the parameters D_1, H_1, D_2, and σ_w.

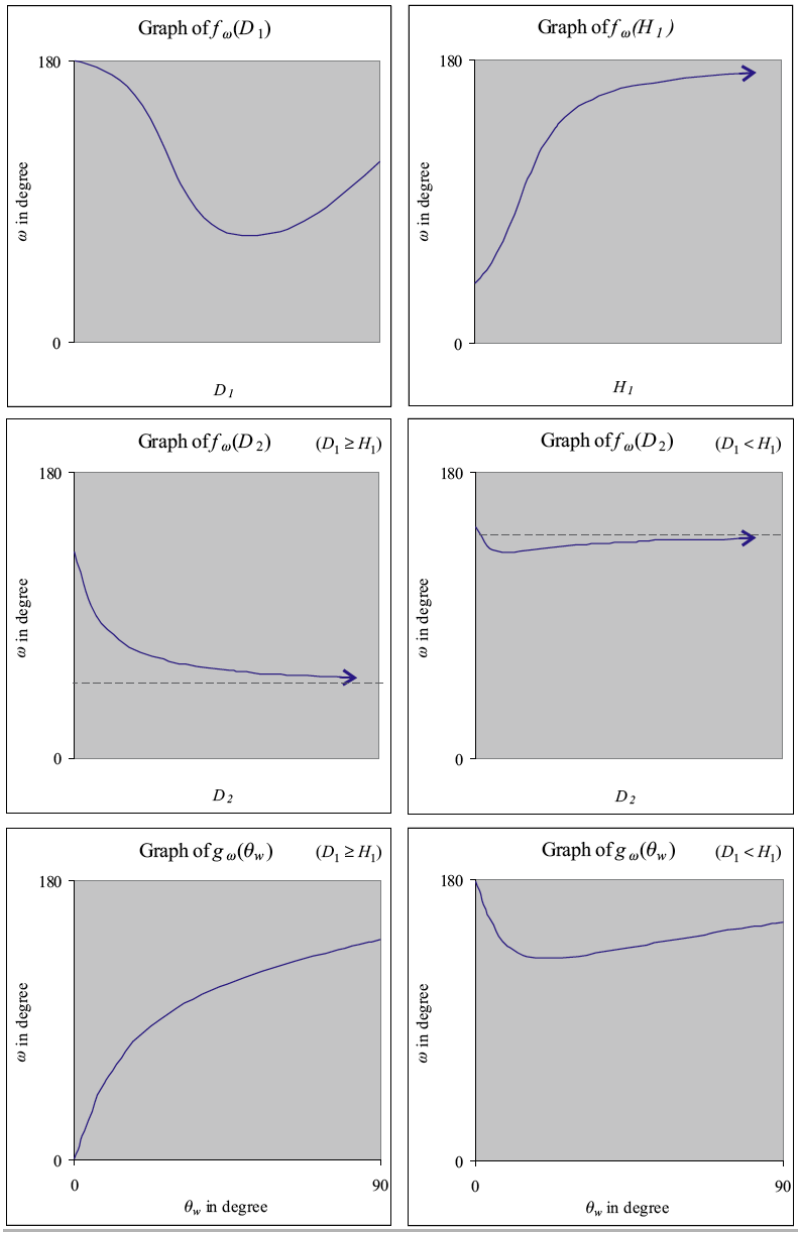

Figure 3.10. Graphs of functions defining ω, each with respect to exactly one of the parameters D_1, D_2, H_1, and σ_w.

Let $f_\omega$be the function for specifying ω with respect to the single variable D_1. Conclusions drawn about near scene range versus principal angle show that $f_\omega$is continuous and has a single minimum on $(0, D_2)$.

Now consider function f_ω with respect to the single variable H_1, see Equation (2). This function is continuous and increasing on $(0, \infty)$.

Let $f_\omega$be the function with respect to the single variable D_2. In case of $D_1 \geq H_1$ it follows that f_ω is continuous and decreasing on (D_1, ∞), and its graph has a horizontal asymptote. In case of $D_1 < H_1$, function $f_\omega(D_2)$ is continuous and has a single minimum on (D_1, ∞).

Finally, consider function f_ω with respect to σ_w, see Equation (9). In case $D_1 \geq H_1$ it follows that f_ω is continuous and increasing on $(0°, 90°)$. For case $D_1 < H_1$, function f_ω is continuous and has a single minimum on $(0°, 90°)$.

Because all the graphs of function f_ω, with respect to any of the four parameters, are either decreasing, increasing, or continuous and have a single minimum, we can again conclude that the maximum value of ω within the bounded region, defined by the cross product of the four intervals $[D_{1min}, D_{1max}]$, $[D_{2min}, D_{2max}]$, $[H_{1min}, H_{1max}]$, and $[\sigma_{wmin}, \sigma_{wmax}]$, lies at one corner of the hypercube. This reduces the search space for the maximum of ω to 16 possible combinations of these endpoints.

Because $f_\omega(H_1)$ is increasing, the maximum of ω is taken for $H_1 = H_{1max}$. This further reduces the search space from 16 points to eight points. Furthermore, if $D_{1min} \geq H_{1max}$, then just one comparison between two values is sufficient to find the maximum of ω. If $D_{1min} \leq H_{1max} \leq D_{1max}$ then the cardinality of the search space is just equal to five.

CONCLUSIONS

The symmetric (or "standard stereo") panorama model appears to be of very basic importance, and we expect that it will be more dominant in future panoramic imaging than recently. A special feature of symmetric panoramas is that epipolar lines are parallel to image rows. This feature permits simplified correspondence analysis algorithms (comparable to the so-called standard epipolar geometry of pinhole images) so that symmetric panoramas are directly stereoscopic-viewable. Its similarity to standard epipolar geometry supports the application of stereo-matching algorithms previously developed for binocular pinhole stereo images.

We also investigated a fundamental geometric problem — how is 3D space sampled by a pair of symmetric panoramas? Sample distribution can be characterized by a set of depth layers, a set of equal-height concentric cylinders whose tops and bottoms are cut off by a co-axis hyperboloid symmetric to the base plane. This statement can also be confirmed by the fact that the epipolar surface of stereo panoramas is a half-hyperboloid, see (Seitz, 2001). An analysis was presented in the thesis on how value changes in camera parameters influence the distribution of (potential) spatial samples. The result can be used as a reference for determining values of camera parameters during image acquisition to ensure a desirable resolution in sampling within a defined depth region. The knowledge of sample distribution is also useful for the analysis of the precision of 3D reconstruction results.

We observed that in the inward case (i.e., $\frac{\pi}{2} < \omega \leq \pi$), a 3D point is sampled up to for four times. For an example, see Figure 4.1. A possible application of this observation is the design of calibration-objects for panoramic camera calibration. An ideal calibration-object would be such that all coded points on its surface appear twice in a single panorama image. This additional information plus the original spatial information (e.g., measured distances between points) should allow improvements in calibration accuracy. Moreover, as already known from pinhole images, camera calibration requires that the projection of a calibration-object covers 'most' of the image to ensure sufficient calibration quality. With respect to this

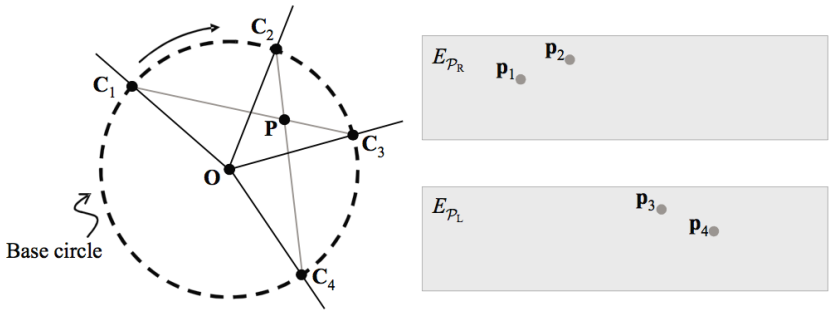

Figure 4.1. A 3D point $\mathbf{P}$ is sampled four times in the inward case. First, by $\mathbf{C}_1$ and $\mathbf{C}_2$, second, by $\mathbf{C}_2$ and $\mathbf{C}_3$, third, by $\mathbf{C}_3$ and $\mathbf{C}_4$, and finally by $\mathbf{C}_4$ and $\mathbf{C}_1$. Point $\mathbf{P}$ appears twice on the right ($E_{\mathcal{P}_R}$), and twice on the left ($E_{\mathcal{P}_L}$) panoramic image respectively.

argument the inward case is more preferable than the outward case (i.e., $0 \leq \omega \leq \frac{\pi}{2}$), because the size of the calibration object may be smaller than R. We believe that the inward case will be of increasing interest, not only for camera calibration as mentioned above but also for reconstructing 3D models of objects.

Given a pair of stereo panoramas with an image resolution $W \times H$, the total number of spatial samples is equal to $W \times H \times \lfloor \frac{\omega W}{\pi} \rfloor$. The off-axis distance R of a stereo panorama pair has no contribution to the spatial sampling resolution. Although the spatial sampling resolution increases while the value of ω increases, the samples are clustered more and more towards the center of the base circle as the value of ω becomes greater than $\frac{\pi}{2}$. This means that although the total number of samples is increasing, the number of samples outside the base cylinder is actually decreasing. It follows that the spatial sampling resolution of a stereo panoramic pair outside of the base cylinder reaches a maximum if $\omega = \frac{\pi}{2}$.

References

Chen, S. E.: QuickTimeVR - an image-based approach to virtual environment navigation. In Proc. *SIGGRAPH*, pages 29–38, 1995.

Howard, I. P., and B. J. Rogers: *Binocular Vision and Stereopsis.* Oxford Psychology Series No.29. Oxford University Press, New York, 1995.

Huang, H.-C., and Y.-P. Hung: Panoramic stereo imaging system with automatic disparity warping and seaming. *Graph. Models Image Processing*, **60**:196–208, 1998.

Huang, F., R. Klette, S. K. Wei, A. Börner, R. Reulke, M. Scheele, and K. Scheibe: Hyper-resolution and polycentric panorama acquisition and experimental data collection. Technical Report, CITR-TR-90, Dept. of Computer Science,The University of Auckland, 2001.

F. Huang and T. Pajdla. Epipolar geometry in concentric panoramas. Research Report CTU–CMP–2000–07, Center for Machine Perception, Czech Technical University, Prague, Czech Republic, March 2000.

Huang, F., S. K. Wei, and R. Klette: Geometrical fundamentals of polycentric panoramas. In Proc. *Int. Conf. Computer Vision*, Volume I, pages 560–565, 2001b.

Huang, F., S. K. Wei, and R. Klette: Stereo reconstruction from polycentric panoramas. In Proc. *Robot Vision*, LNCS 1998, pages 209–218, 2001c.

Huang, F., S. K. Wei, and R. Klette: Rotating line cameras: model and calibration. Institute for Mathematics and its Applications, University of Minnesota, IMA Preprint Series, report 2104 (64 pages), March 2006.

Huang, F., S. K. Wei, and R. Klette: Rotating line cameras: Epipolar geometry and spatial sampling. Institute for Mathematics and its Applications, University of Minnesota, IMA Preprint Series, report 2105 (46 pages), March 2006.

Ishiguro, H., M. Yamamoto, and S. Tsuji: Omni-directional stereo. *IEEE Trans. Pattern Analysis Machine Intelligence*, **14**:257–262, 1992.

Kang, S.-B., and P. K. Desikan: Virtual navigation of complex scenes using clusters of cylindrical panoramic images. Technical Report, CRL 97/5, Digital Equipment Corporation, Cambridge Research Lab, 1997.

Kang, S.-B., and R. Szeliski: 3-d scene data recovery using omnidirectional multibaseline stereo. *Int. J. Computer Vision*, **25**:167–183, 1997.

Kang, S.-B., and R. Weiss: Characterization of errors in compositing panoramic images. In Proc. *Computer Vision Pattern Recognition*, pages 103–109, 1997.

Mayer, U., M. D. Neumann, W. Kubbat, and K. Landau. Is eye damage caused by stereoscopic displays? In Proc. *SPIE Stereoscopic Displays Virtual Reality Systems.* pages 4–11, 2000.

McMillan, L., and G. Bishop: Head-tracked stereo display using image warping. In Proc. *Stereoscopic Displays Virtual Reality Systems*, SPIE-2409, pages 21–30, 1995.

McMillan, L., and G. Bishop: Plenoptic modeling: an image-based rendering system. In Proc. *SIGGRAPH*, pages 39–46, 1995a.

Murray, D.W.: Recovering range using virtual multicamera stereo. *Computer Vision Image Understanding*, **61**:285–291, 1995.

Peleg, S., and M. Ben-Ezra: Stereo panorama with a single camera. In Proc. *Computer Vision Pattern Recognition*, pages 395–401, 1999.

Peleg, S., Y. Pritch, and M. Ben-Ezra: Cameras for stereo panoramic imaging. In Proc. *Computer Vision Pattern Recognition*, pages 208–214, 2000.

Rademacher, R., and G. Bishop: Multiple-center-of-projection images. In Proc. *SIGGRAPH*, pages 199–206, 1998.

Reulke, R., and M. Scheele: Der Drei-Zeilen CCD-Stereoscanner WAAC: Grundaufbau und Anwendungen in der Photogrammetrie. *Photogrammetrie Fernerkundung Geoinformation*, **3**:157–163, 1998.

Roberts, J. W., and O. T. Slattery: Display characteristics and the impact on usability for stereo. In Proc. *SPIE Stereoscopic Displays Virtual Reality Systems*, pages 128–137, 2000.

Scheibe, K., H. Korsitzky, and R. Reulke: Eyescan - a high resolution digital panoramic camera. In Proc. *Robot Vision*, pages 77–83, 2001.

Seitz, S.M.: The space of all stereo images. In Proc. *Int. Conf. Computer Vision*, pages 26–33, 2001.

Shum, H.-Y., and L.-W. He: Rendering with concentric mosaics. In Proc. *SIGGRAPH*, pages 299–306, 1999.

Shum, H., A. Kalai, and S. Seitz: Omnivergent stereo. In Proc. *Int. Conf. Computer Vision*, pages 22–29, 1999.

Shum, H.-Y., and R. Szeliski: Stereo reconstruction from multiperspective panoramas. In Proc. *Int. Conf. Computer Vision*, pages 14–21, 1999.

Siegel, M., and S. Nagata: Just enough reality: comfortable 3-d viewing via microstereopsis. *IEEE Trans. Circuits Systems Video Technology*, **10**:387–396, 2000.

Siegel, M., Y. Tobinaga, and T. Akiya: Kinder gentler stereo. In Proc. *SPIE Stereoscopic Displays and Applications*, pages 18–27, 1999.

Szeliski, R., and H.-Y. Shum: Creating full view panoramic image mosaics and environment maps. In Proc. *SIGGRAPH*, pages 251–258, 1997.

Valyrus, N. A.: *Stereoscopy.* Focal Press, London, 1966.

Viire, E.: Health and safety issues for VR. *Comm. ACM*, **40**:40–41, 1997.

Ware, C., C. Gobrecht, and M. Paton. Dynamic adjustment of stereo display parameters. *IEEE Trans. Systems Man Cybernetics*, **28**:56–65, 1998.

Wei, S. K., F. Huang, and R. Klette: Three dimensional view synthesis from multiple images. Technical Report, CITR-TR-42, Dept. of Computer Science, The University of Auckland, Auckland, 1999a.

Wei, S. K., F. Huang, and R. Klette: Determination of geometric parameters for stereoscopic panorama cameras. *Machine Graphics & Vision*, **10**:399–427, 2002a.

Werner, T., and T. Pajdla: Cheirality in epipolar geometry. In Proc. *Int. Conf. Computer Vision*, pages 548–553, 2001.

Yamanoue, H., M. Okui, and I. Yuyama: A study on the relationship between shooting conditions and cardboard effect of stereoscopic images. *IEEE Trans. Circuits Systems Video Technology*, **10**:411–416, 2000.